CHALMERS
UNIVERSITY OF TECHNOLOGY

Automatic detection of boats in underwater recordings

Master's thesis in Master Programme Sound and Vibration

Theresia Muhr

DEPARTMENT OF ARCHITECTURE AND CIVIL ENGINEERING

CHALMERS UNIVERSITY OF TECHNOLOGY
Gothenburg, Sweden 2025
www.chalmers.se

Master's thesis 2025

Automatic detection of boats in underwater recordings

Theresia Muhr

CHALMERS
UNIVERSITY OF TECHNOLOGY

Department of Architecture and Civil Enineering
Division of Applied Acoustics
Chalmers University of Technology
Gothenburg, Sweden 2025

Automatic detection of boats in underwater recordings
Theresia Muhr

Supervisor: Torbjörn Johansson, IVL Svenska Miljöinstitutet
Examiner: Jens Forssén, Architecture and Civil Engineering

Master's Thesis 2025
Department of Architecture and Civil Engineering
Division of Applied Acoustics
Chalmers University of Technology
SE-412 96 Gothenburg
Telephone +46 31 772 1000

Cover: Recreational boats, moored at the dock in Rörö harbour.

Typeset in LaTeX
Printed by Chalmers Reproservice
Gothenburg, Sweden 2025

Automatic detection of boats in underwater recordings
Theresia Muhr
Department of Architecture and Civil Engineering
Chalmers University of Technology

Abstract

The research addresses a growing environmental challenge in Swedish coastal waters, where increasing recreational boat traffic poses risks to marine ecosystems through underwater noise pollution [1]. While commercial vessels can be tracked through AIS transponders, the vast majority of recreational boats operate without monitoring systems [2], leaving a significant gap in our understanding of their environmental impact. To address this challenge, an automated detection system using underwater acoustic recordings was developed to identify and quantify recreational boat presence in coastal waters.

Building on established signal processing techniques, a detection system based on the short-time-average/long-time-average (STA/LTA) algorithm was implemented [3]. The focus is on optimizing three key components: bandpass filtering parameters, window functions, and detection thresholds. During fieldwork in August 2024, continuous underwater recordings along the Swedish coast were collected using SoundTrap and RTsys hydrophones. To validate the system's performance, Reciever Operating Characteristic (ROC) curves were used [4] to fine-tune the detection parameters for optimal sensitivity while minimizing false positives.

Through systematic testing, an STA of 3 minutes and an LTA with the same length as the recording were found to yield the best performance. The frequency band of 100 Hz to 4000 Hz showed the highest effectiveness in detecting vessel noise. Threshold optimization revealed that values below 0.5 minimize missed detections, while values above 0.8 reduce false positives, establishing an optimal operating range of 0.5 to 0.8. These values were obtained from recordings containing numerous boat passages. They may vary for recordings with fewer passages.

The resulting energy detector offers a practical and adaptive solution for monitoring recreational boat activity. These findings enhance the ability to quantify anthropogenic noise in marine environments and provide a foundation for informed environmental protection efforts.

Keywords: boat detection, underwater acoustics, energy detection, signal processing, environmental monitoring, recreational vessels, coastal waters, noise pollution

Acknowledgements

I want to express my deepest gratitude to everyone who supported me throughout the process of writing this thesis.
First and foremost, I am incredibly thankful to my supervisor, Torbjörn Johansson, at IVL Swedish Environmental Research Institute. His invaluable guidance, thoughtful feedback, and unwavering encouragement were instrumental in shaping this work. I am also deeply grateful to his colleague, Carl Andersson, for his continuous support and for generously sharing his expertise, which played a significant role in the success of this thesis.
I would also like to extend my heartfelt thanks to my examiner, Jens Forssén, from the Division of Applied Acoustics at Chalmers University of Technology. His thoughtful supervision and constructive suggestions during our meetings were crucial in guiding the direction of my research.
My gratitude also goes to the Acoustics Team at IVL. Their collaboration and support throughout this process were invaluable, and I truly appreciated their willingness to assist whenever I needed help.
A special thank you to Engineers of Sweden for awarding me the Sveriges Ingenjörers Miljöfond Scholarship. This generous support allowed me to dedicate myself fully to my research on environmental acoustics, contributing to the foundation's mission of promoting solutions for improving Sweden's physical environment.
I am profoundly grateful to my family, whose love and encouragement have been my anchor throughout this journey. Their unwavering belief in me gave me the strength to overcome every challenge. A special thank you to my partner, whose patience, understanding, and constant support made all the difference during this process.
Finally, I want to thank my friends, colleagues, and everyone who has been part of my journey. Your companionship and support, both academically and personally, have been a constant source of motivation, and I am truly fortunate to have you by my side.

Theresia Muhr, Gothenburg, June 2025

List of Acronyms

Below is the list of acronyms that have been used throughout this thesis, listed in alphabetical order:

ADC	Analog-to-Digital Converter
AIS	Automatic Identification System
AUC	Area Under the Curve
dB	Decibel
DFT	Discrete Fourier Transform
ED	Energy Detector
FFT	Fast Fourier Transform
FPR	False Positive Rate
LTA	Long-Term Average
Pa	Pascal
PSD	Power Spectral Density
ROC	Receiver Operating Characteristic
SPL	Sound Pressure Level
STA	Short-Term Average
TPR	True Positive Rate

Nomenclature

Below is the nomenclature of indices, sets, parameters, and variables that have been used throughout this thesis. Units are included for all quantities where applicable for clarity.

Indices

n	Index for angles in Snell's Law and for time-domain samples in FFT (unitless)
i	Index for different signal processing windows (unitless)
r	Range in meters for transmission loss (m)
f	Frequency index in equations (unitless)
c_1, c_2	Speed of sound in different media (m/s)

Sets

$\mathcal{T}$	Set of temperature values at different depths (°C)

Parameters

p_{ref}	Reference pressure ($1\,\mu$Pa)
c	Speed of sound in water (m/s)
ρ	Density of water (kg/m^3)
ρ_1, ρ_2	Densities of the first and second medium (kg/m^3)
α	Absorption coefficient (dB/m)
SS	Spherical spreading loss (dB)
PL	Propagation loss (dB)
Z	Acoustic impedance (Pa $\cdot$ s/m)

T	Temperature (°C)
S	Salinity (g/kg)
z	Depth (m)
N	Number of samples in the signal (unitless)

Variables

p	Measured pressure (Pa)
SPL	Sound pressure level (dB re $1\,\mu$Pa)
f	Frequency of sound wave (Hz)
θ_1, θ_2	Incident and refracted angles (degrees or radians, depending on context)
r	Distance from the sound source (m)
E	Energy of a detected signal ($\text{Pa}^2 \cdot \text{s}$)
PL	Propagation loss at distance r (dB)
Z_1, Z_2	Acoustic impedances of different media ($\text{Pa} \cdot \text{s/m}$)
x_n	Discrete-time signal sample at index n (Pa or unitless depending on scaling)
$X(\omega)$	Discrete Fourier Transform (DFT) of x_n (complex-valued, unit depends on x_n)
$P(\omega)$	Power spectrum at frequency ω (Pa^2/Hz or dB)
ω	Normalized angular frequency (rad/sample)
R	Reflection coefficient (dimensionless)
T_r	Transmission coefficient (dimensionless)

Contents

List of Figures

List of Tables

1
Introduction

Due to Sweden's geographical location, it has beautiful and long coastal areas with shallow waters and small islands that create picturesque conditions for recreational boat users. These areas are a flourishing environment for vegetation such as seagrass, pondweed, and stoneworts that are the feeding grounds and homes of a high biological diversity of fish and invertebrates [1].

In Sweden alone, there are 700000 recreational boats, one of the highest numbers worldwide relative to its population [2]. The number of docks necessary to hold these boats increased compared to the 1960s, with almost 160 % [1]. The demand for docks is growing alongside the number of recreational boats, which make up the majority of maritime traffic in these regions. In contrast to commercial vessels, which are closely monitored, only a small number of recreational boats are equipped with Automatic Identification System (AIS) transponders, leaving most of them unmonitored.

The increases in general boat traffic are related to the rise in the ambient underwater noise level [5]. In shallow coastal zones, the greatest influence on the background noise level was the presence of recreational boats [6]. When boats move through water, they generate noise due to cavitation at the propeller and their engine, which is rigidly mounted to the hull [2].

The hearing ranges of marine mammals, fish, and invertebrates overlap with the frequency range of underwater noise due to boating activity. This disturbs their ability to navigate, feed, mate, and communicate [7]. Seals can experience temporary or permanent shifts in their auditory threshold when exposed to too loud noise [8, 5].

The attempts to protect marine life prioritize commercial shipping, but at the same time, they fail to adequately address noise from recreational boats, despite their prevalence in coastal areas [2]. The absence of effective monitoring tools results in a gap in environmental protection for these regions. Without comprehensive monitoring, the environmental impact of boat noise is likely to worsen [7].

In this thesis, an automated system was developed using energy detection. It utilizes underwater sound recordings to detect and quantify the presence of recreational boats. The system was optimized by evaluating key signal processing parameters, including window lengths, bandpass filters, and detection thresholds using Receiver Operating Characteristic (ROC) curves.

This will allow authorities to understand and track recreational boat traffic. It will help to conclude the environmental impact that these recreational boats cause. This tool will provide environmental agencies with actionable data on noise pollution, supporting their efforts to mitigate environmental harm in vulnerable coastal areas.

This thesis is structured as follows: Chapter 2 reviews related work and relevant signal processing methods. Chapter 3 details the methodology used for data collection and detection system development. Chapter 4 presents the results of the optimization process, and Chapter 5 discusses their implications. Finally, Chapter 6 concludes with a summary of key findings and future research directions.

2

Theory

This chapter provides an overview of underwater acoustics, including key principles and units. It explains different noise sources and the generation of underwater noise, followed by an introduction to signal processing techniques such as windowing and energy detection. Lastly, the Receiver Operating Characteristic (ROC) curves are discussed, which are used to validate the settings in the energy detection algorithm.

2.1 Sound Propagation and Acoustic Principles

This section introduces the underwater acoustic environment, highlighting key physical principles and phenomena that explain sound propagation in water. Underwater acoustics, or hydroacoustics, is the study of how sound is produced, travels through, and is detected in water-based environments. It plays a critical role in applications such as sonar systems, underwater communication, and environmental monitoring. A solid understanding of foundational concepts like acoustic impedance, reflection, refraction, absorption, and sound channels is essential for interpreting underwater sound behavior.

2.1.1 Sound Pressure and Decibels

Sound propagation underwater follows a similar principle to that in air. The wave propagation is caused by particle oscillations that transport energy through the medium [9]. The quantity used to describe the strength of sound is pressure, and is measured in Pascals (Pa). Because the range of sound pressure is very wide, it is commonly expressed on a logarithmic scale using decibels (dB). This simplifies comparisons and better reflects the human perception of sound levels. The sound pressure level (SPL) is the force per unit area and is defined as follows:

$$\text{SPL (in dB)} = 10\log_{10}(p^2/p_{ref}^2) = 20\log_{10}(p/p_{ref}) \tag{2.1}$$

where p is the pressure with its unit Pascal (Pa) and p_{ref} is the reference pressure. For hydroacoustics, the reference pressure is 1 μPa, which is 10^{-6} Pa. The SPL represents the sound pressure expressed in dB relative to this reference level [10].

2.1.2 Speed of Sound and Influencing Factors

The speed of sound in water, c, has the unit (m/s) and is a function of temperature, T, salinity, S, and ambient pressure expressed through the depth, z. The sound speed increases with both T, S and z [10]. The formula used for its calculation can be seen in equation 2.2.

$$c = 1449.2 + 4.6T - 0.055T^2 + 0.00029T^3 + (1.34 - 0.01T)(S - 35) + 0.016z \quad (2.2)$$

The temperature is measured in degrees Celsius. During warmer periods, its value is higher near the surface, and it then reduces with depth until it stays at a constant value. In cold periods, its value is similar from the sea surface to higher depths. The pressure increases constantly with depth, and the salinity is often almost the same, even at higher depths. A sketch of how these three typically behave is shown in Figure 2.1. The value of the speed of sound can range from 1450 m/s to 1540 m/s [11, 12].

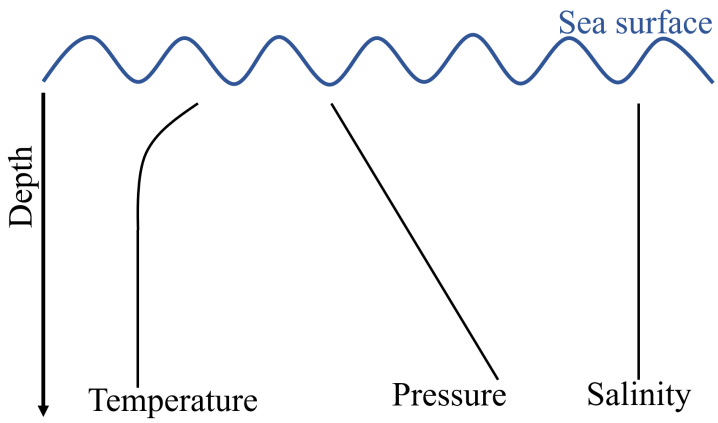

Figure 2.1: Sketch of the changes of temperature, pressure, and salinity with depth.

2.1.3 Propagation Loss and Attenuation

Understanding sound propagation underwater requires not only defining its strength using decibels but also considering how sound attenuates as it moves through the ocean. Sound attenuates as the range from the source increases due to two physical effects, absorption and spreading. Higher frequencies experience more absorption than lower frequencies, propagating further in water. The simplest form of spreading is spherical spreading, in which sound spreads equally in all directions. The combined effect of absorption and spreading is called propagation loss, PL, it's a measure that describes the signal's weakening as it propagates away from the source [13]. The propagation loss can be calculated using the absorption coefficient, α, and the spherical spreading factor, SS, as follows:

$$\alpha = \frac{0.11\ f^2}{1+f^2} + \frac{44\ f^2}{4100+f^2} + 2.75 \cdot 10^{-4}\ f^2 + 0.003\ \text{(dB/km)} \tag{2.3}$$

$$SS = 20 \log r \quad \text{(dB)} \tag{2.4}$$

$$PL = SS + \alpha \cdot r \cdot 10^{-3} \quad \text{(dB)} \tag{2.5}$$

For calculating the absorption coefficient, α, using equation 2.3, f is the frequency in (kHz). Equation 2.4 shows how to calculate the spherical spreading with r being the range in meters. Those two are needed to calculate the propagation loss, PL, using equation 2.5 [12].

2.1.4 Acoustic Impedance and Reflection

To understand reflection in acoustics, looking at the impedance, Z, of a medium is necessary. For a simple plane wave, it can be calculated using equation 2.6.

$$Z = \rho \cdot c \tag{2.6}$$

In the equation for calculating the impedance, the density, ρ, is multiplied by the speed of sound, c. It is also referred to as the "acoustic impedance". In air at atmospheric pressure and a temperature of 20°C the density, ρ_0, is 1.21 kg m^{-3} and the speed of sound, c_0 is 343 m/s. In freshwater at the surface and a temperature of 20°C the speed of sound, c_0 is 1480 m/s and the density, ρ_0 is 1000 kg m^{-3} which results in an impedance of 1.48×10^6 kg $m^{-2}s^{-1}$ [14].

The change of impedance from one medium to another results in reflection. The degree of reflection and transmission at a boundary depends on the ratio of the acoustic impedances of the two media. These differences are often referred to as the impedance mismatch [10]. This mismatch happens at the sea surface and the sea bed.

At the sea surface, there is a high impedance mismatch, which results in almost all of the sound energy being reflected into the sea [12]. Since the sea surface is often rough, this scatters sound in directions away from the specular reflecting angle. These reflections cause constructive and destructive interference due to a phase change.

When the sound wave interacts with a boundary, Fresnel's equations describe how much of the wave is reflected or transmitted. This is determined by the acoustic impedance of the media and calculated using reflection and transmission coefficients. The equation for the reflection coefficient is given in equation 2.7, and the calculation for the transmission coefficient is given in equation 2.8. They describe the energy reflection and transmission coefficients assuming that the acoustic impedances Z_1

and Z_2 are real-valued. They neglect possible losses due to absorption or other dissipative effects.

$$R = \left(\frac{Z_2 - Z_1}{Z_2 + Z_1}\right)^2 \tag{2.7}$$

$$T_r = 1 - R = \frac{4Z_1Z_2}{(Z_1 + Z_2)^2} \tag{2.8}$$

Here $Z_1 = \rho_1 c_1$ and $Z_2 = \rho_2 c_2$ are the acoustic impedances of the two media, R is the reflection coefficient (part of the energy that got reflected), T is the transmission coefficient (the fraction transmitted), ρ is the density and c is the speed of sound in each medium.

These equations illustrate the amount of energy reflected and transmitted at the boundary due to an impedance mismatch (in this case, the water surface) [10].

2.1.5 Refraction and Snell's Law

In addition to reflection, a portion of the wave may also be transmitted into the second medium and refracted. This behavior is explained by Snell's Law. The angle in which the reflections occur can be calculated using equation 2.9).

$$\frac{\sin\theta_1}{c_1} = \frac{\sin\theta_2}{c_2} \tag{2.9}$$

Here c_n represents the two different sound speeds and $\sin\theta_n$ the two different angles of incidence and refraction.

When a sound wave hits a boundary between two media with different sound speeds, a part of the wave is reflected and a part is refracted (transmitted). The refraction angles follow Snell's Law (see equation 2.9). It relates the angles of incidence and transmission to the sound speeds in each medium [15, 9].

2.1.6 The Lloyd Mirror Effect

The constructive and destructive interference between the direct path and the surface-reflected path leads to the Lloyd mirror effect, a phenomenon often visible in spectrograms of underwater recordings. Figure 2.2 shows this example with two boat passages. It appears as a characteristic U-shaped pattern caused by the frequency-dependent phase difference between the two paths.
What happens to the sound waves at the ocean bottom is more complicated; it is a rough layered structure that can be made out of mud, sand, gravel, and rocks. Those materials all have different acoustic impedance. Mud, for example, has a similar impedance to water, so it transmits sound easily. Rock, on the other hand, has a higher acoustic impedance, so it reflects more. The sea bed can be constructed

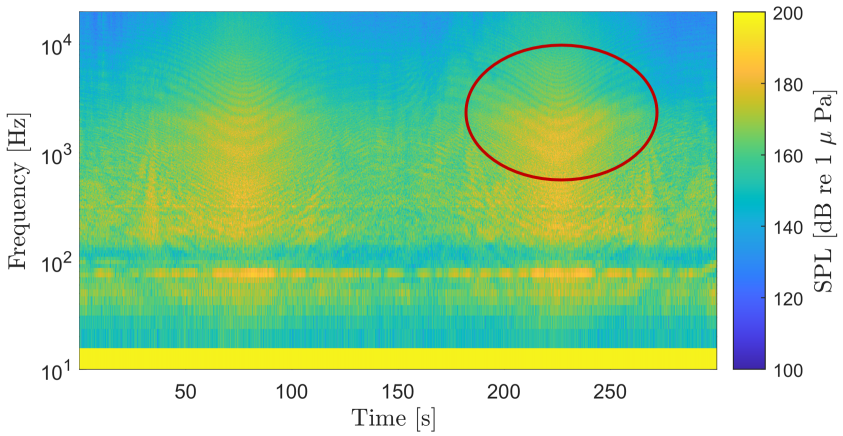

Figure 2.2: Example of the Lloyd mirror effect with two boat passages.

out of different layers and therefore sometimes absorb or reflect sound more [10].

2.1.7 Sound Channel

Knowing about the speed of sound underwater and the reflective properties, due to their change, is necessary to understand the sound channel. In the sound channel, waves can travel long distances with minimal loss. This is only true for deep waters. It forms due to the changing sound speed with depth. Looking back at Figure 2.1 in Section 2.1.1, the combination of the three sketched lines for temperature, pressure, and salinity results in the profile of the speed of sound. A sketch for this can be seen in Figure 2.3a.

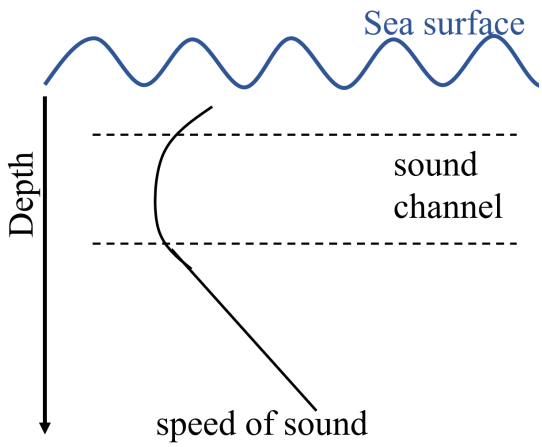

(a) Sketch of how the speed of sound varies with depth and the sound channel.

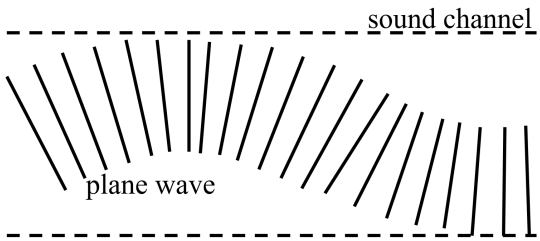

(b) Sketch of a plane wave propagating in the sound channel, idealized representation.

Figure 2.3: Comparison of sound speed variation with depth and plane wave propagation in the sound channel.

When a plane wave propagates through the sound channel upwards, it reaches layers where the speed of sound is higher, so it gets refracted back downwards. When traveling downward, the plane waves hit denser water with higher pressure and get refracted upward. This "traps" the plane waves in the sound channel between these layers, bouncing up and down in a duct-like path (see figure 2.3b) [16].

These propagation effects, reflection, refraction, and channeling, directly influence how sound waves behave in shallow and deep waters. They form the acoustic basis for signal detection explored later in this thesis.

2.2 Underwater noise sources

The underwater soundscape was, before the industrial revolution, composed of sounds from geological, biological, and meteorological sources with minor contributions from human sources [17]. With growing industrialization, the shipping traffic has also grown, leading to a noisier soundscape underwater. In the following, the anthropogenic and ambient sound sources are presented, and the sound generation of these will be explained.

2.2.1 Anthropogenic sounds

Anthropogenic sound events are human-induced; they can originate intentionally or unintentionally as a by-product of other activities. Intentionally produced sounds are for example explosions, seismic exploration, sonars, and acoustic deterrent devices. Sounds that are unintended by-products include shipping noise and industrial activities. These sounds create noise pollution, which causes local disturbances that are high in level as well as a continous low-level and frequency background noise that can travel far in the waters. Locations with high levels of underwater noise are typically along shipping routes and particularly encompass coastal regions [18].

The frequency spectrum of noise radiated from boats and ships varies with their vessel type, so its characteristics are hard to predict. Commercial shipping is usually the cause of chronic low-frequency background noise; when this noise enters the sound channel, it can travel more than 1000 km and still be detected [16]. Recreational boats cause more local disturbances since no sound channel can form in shallow waters where they travel. After approximately 3 km the sound of smaller vessels is attenuated so it is not measureable anymore [17].

The two main contributors to the noise of boats are the propeller and the engine. Cavitation is the main mechanism for the dominant noise from the propeller, generated at higher loads. As the propeller rotates, pressure differences between the leading and following surfaces of the blade create regions of high and low pressure [19].

When the torque on the propeller is high enough, the pressure on the trailing surfaces of the blades drops below the vapor pressure of water. This causes cavitation, a process in which water vaporizes at ambient temperature, forming bubbles filled with steam. These bubbles collapse as they move into regions with higher pressure. Due to the different sizes of the bubbles filled with steam, they have different lifetimes, which results in a broadband noise [20]. The tonal components in its spectrum are related to the blade passing frequency and higher harmonics.

The ship's engine is the other main contributor to its radiated sound. The most dominant sources are often diesel engines that are mounted rigidly on a structure that is connected to the hull of the ship. The hull then acts as a membrane that radiates the energy into the sea [21, 22].

The frequency spectrum of small recreational vessels varies with speed and distance [23]. If the boat is further away from the receiver, due to propagation loss, less of the high-frequency signal reaches it. Regarding the speed, one can see in figure 2.4 that with low speed (3 knots), the main share of the energy is located at low frequencies (approximately 50 Hz in this case). When the speed increases, the energy spreads out over a larger frequency range. With the speed of 10 knots, the significant part of the energy spreads until approximately 6 kHz. This vessel is picked as an example to visualize the speed dependence. The recordings were made by IVL and Björn Wrede at Lifestyle Boating AB near Havstenssund in May 2024.

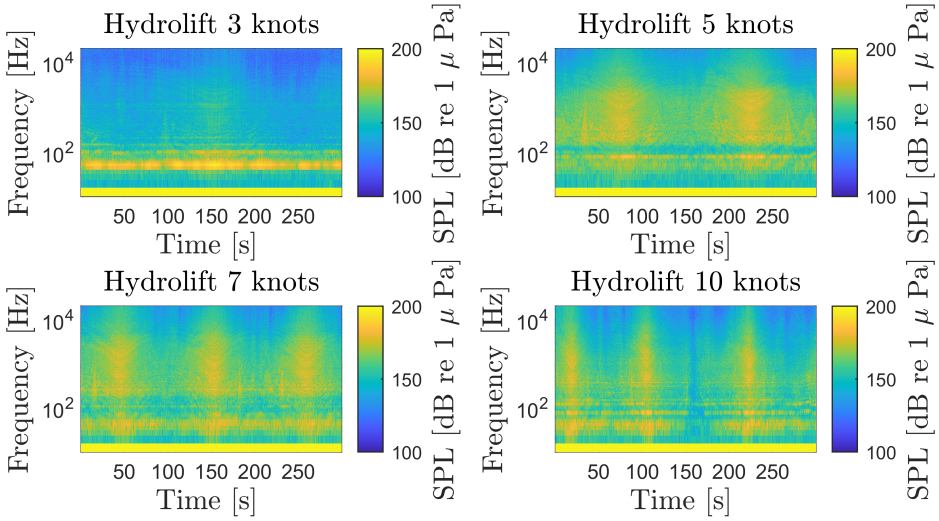

Figure 2.4: Spectrogram of the boat "Hydrolift" with four different speeds.

2.2.2 Ambient sounds

Similar to our living environment, natural ambient noise has always formed the baseline noise floor, acting as a limiting factor for the detection of weaker signals. Since the Industrial Revolution, the background noise level has risen due to transport machinery. The ambient noise field depends on the strength and density of sources, as well as the propagation to the receiver. The underwater environment is also a

contributing factor with its sound speed, the acoustic properties of the seabed, and ocean dynamics. The differences in level of underwater ambient noise are large and depend on time, location, and depth. Ambient sources of noise include processes of waves, rain, bio-acoustic sound generation, earthquakes, and thermal agitation of the seawater [7].

In shallow water, ambient noise interacts with the seabed. Its structure is crucial to its influence on the sound. Usually, the seabed has a moderate reflectivity, which results in ambient noise reflecting back and forth between the seabed and the surface, resulting in higher ambient noise levels (approximately 5 dB) compared to deep water [24].

Depending on the wind speed, the wind-generated sea surface agitation covers frequencies between 200 Hz up to approximately 100 kHz [25]. It is due to bubbles bursting created in the process of waves breaking. At low frequencies, bubble clouds (groups of bubbles) oscillate together as a whole. This movement generates low-frequency sound waves. At higher frequencies, the sound is produced by individual bubbles oscillating at their natural resonance frequency. Due to the frequency-dependent propagation loss in water, the high-frequency sounds from individual bubbles are more local [26].

For rain, the noise is generated due to the impact of raindrops on the sea surface. They trap air and generate bubbles that oscillate at their resonance frequency. It can produce a peak in the ambient sound around 15 kHz for rain rates of 2 mm/hr to 5 mm/hr. At higher rain rates, the spectrum flattens out and can reach the level of 80 dB (re 1 μPa) at 10 kHz [27].

2.3 Digital Signal Processing

As described in section 2.1.1, sound is a form of transported energy. This energy can be detected by microphones in the air or hydrophones underwater. These hydrophones translate the pressure into a continuous voltage signal. A signal which is continous can have a value at any moment in time. This value can be any real number within a certain range. The range gets defined by the maximum and minimum value of the signal, as the highest and lowest pressure in it. In between those limits can be infiniety many values, characterizing the signal. To be able to process these signals with a computer, they must be converted from analog to digital signals [28]. This is done using an analog-to-digital converter (ADC), which takes information out of the analog signal at discrete time steps and quantizes it into a finite number of levels. The sampling rate must be at least twice the highest frequency component of the signal to prevent aliasing (Nyquist theorem).

2.3.1 Bandpass

The bandpass filter is used to focus on the dominant frequency range in which boats emit noise. This helps to reduce the intensity of the background noise. A bandpass

filter passes the frequencies between two cutoff frequencies, the lower limit and the upper limit. The other content is attenuated or removed. It can be a combination of a low-pass filter and a high-pass filter in series. The cutoff frequency of the high-pass filter is the lower limit, and the cutoff frequency of the low-pass filter is the higher limit. The difference between these two frequencies determines the bandwidth [29]. The filter order determines how steep the transition is between the passband and stopband. A lower order enables a smoother transition at the frequency limits. The transition determines how much energy of the frequencies to the side still gets added to the filtered signal. A first-order filter has a decrease of -6 dB per octave, and a second-order filter decreases at -12 dB per octave. The Butterworth filter is considered a good practical filter due to its smooth frequency response in the passband [30]. Although it is not ideal in the strict sense, since ideal filters are not physically realizable, it is widely used because of its flat passband characteristics.

2.3.2 Windowing

Windowing is necessary to divide the input signal into smaller segments (blocks), which are then analyzed. For this, each segment is multiplied by a window function before further processing. This technique is used in energy detection to isolate events for further calculations [29].

The Discrete Fourier Transform (DFT) assumes that the analyzed signal is periodic and repeats infinitely. If the beginning and the end of a finite signal segment do not match, it creates a discontinuity at the edges of the repeated signal, which leads to spectral leakage, a spreading of energy from strong frequency components into neighbouring bins. This can overshadow weaker signals. Applying a window function helps to reduce spectral leakage by smoothing the signal edges, even though it also slightly reduces spectral resolution [31].

The basic window is the rectangular window. Due to its shape, it's also called a uniform window or a box car window. Its mathematical expression can be seen in equation 2.10. The von Hann window (see equation 2.11) has, in comparison to the rectangular window, significantly reduced side lobes but at the expense of double the main-lobe width. The Blackman-Harris window achieves a trade-off between the main-lobe width and the side-lobe level. Its mathematical representation can be seen in equation 2.12 with the coefficients a_0, a_1, a_2, a_3 which are chosen to optimize the side-lobe suppression [32].

$$w[n] = 1, \quad 0 \leq n \leq N-1 \tag{2.10}$$

$$w[n] = 0.5\left(1 - \cos\left(\frac{2\pi n}{N-1}\right)\right) \tag{2.11}$$

$$w[n] = a_0 - a_1\cos\left(\frac{2\pi n}{N-1}\right) + a_2\cos\left(\frac{4\pi n}{N-1}\right) - a_3\cos\left(\frac{6\pi n}{N-1}\right) \tag{2.12}$$

where the coefficients are typically chosen as:

$$a_0 = 0.35875,$$
$$a_1 = 0.48829,$$
$$a_2 = 0.14128,$$
$$a_3 = 0.01168.$$

In Figure 2.5, the three windows are shown in comparison, the red dashed line shows the main-lobe width. One can see that the main lobe width is the smallest for the rectangular and the widest for the Blackman-Harris. In comparison, the side-lobe level is the highest for the rectangular window and the lowest for the Blackman-Harris. Greater suppression of spectral leakage leads to lower frequency resolution, which means that closely spaced frequency components become harder to distinguish. The choice of a window function depends on the application. The rectangular window is best for signals with well-separated frequency components (the more they are separated from each other, the less of a problem is the spectral leakage caused by the window). The von Hann window is a good compromise commonly used for speech and audio processing. The Blackman-Harris window is used where minimal spectral leakage is wished, for example, in high-precision frequency analysis [31, 32].

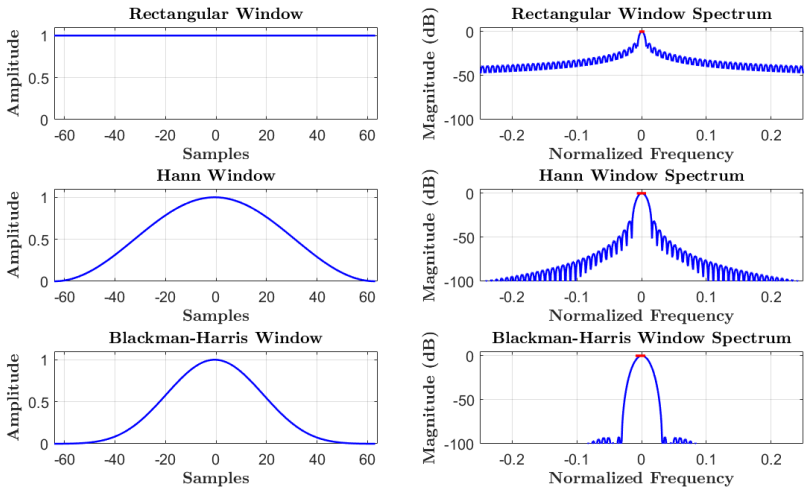

Figure 2.5: Rectangular, von Hann, and the Blackman-Harris window in comparison.

2.3.3 Fast-Fourier-Transform

The Fourier Transform was named after Jean-Baptiste Joseph Fourier and is a mathematical method to analyze the frequency content of a signal. It was originally introduced through the Fourier series in 1822; since then, it has become a fundamental tool in signal processing. Typically used is the Discrete Fourier Transform (DFT), which is applied to discrete signals. The Fast Fourier Transform (FFT) is an implementation of the DFT that is computationally more efficient since it has

fewer required operations. This saves time, especially for large datasets.

The primary function of the FFT is to convert a signal from the time domain (where it represents the amplitude over time) into the frequency domain (where it shows the present energies per frequency). This is useful for identifying patterns or features within a signal that are not easily visible in the time domain [33].

Mathematically, the Discrete Fourier Transform (DFT) is expressed as:

$$X(\omega) = \sum_{n=0}^{N-1} x_n e^{-j\omega n} \tag{2.13}$$

Here, x_n represents the discrete-time input signal, $X(\omega)$ is its frequency-domain representation, N is the total number of samples, and ω is the normalized angular frequency. The result $X(\omega)$ is typically referred to as the signals spectrum. It reveals how much of each frequency is present in the signal.

In applications, especially in audio analysis and detection algorithms, the FFT is used to compute the power spectrum. This is done by taking the squared magnitude of the FFT output:

$$P(\omega) = |X(\omega)|^2 \tag{2.14}$$

In underwater acoustics, the sound pressure signal, $p(t)$, is first sampled into a discrete-time signal, $x[n]$, which represents the same physical pressure values in a digital form. The FFT is applied to $x[n]$ to calculate the frequency-domain signal $X(\omega)$. The power spectrum (equation 2.14) corresponds to the distribution of acoustic energy across frequency, and is therefore proportional to the square of the pressure signal p^2. This reflects the same pressure-squared dependence seen in the definition of SPL (see equation 2.1), establishing a direct link between time-domain pressure signals and their frequency-domain energy representation. While SPL gives a scalar measure of acoustic intensity, the power spectrum reveals how this energy is distributed over frequency and is directly used in the energy detector algorithm later in this thesis.

This spectrum reflects the energy content at different frequencies and allows an examination of the signal's spectral characteristics. This is useful in tasks as filtering, detection of tonal components, noise analysis, or, as in this thesis, energy detection for identifying transient acoustic events [34].

To minimize spectral leakage and improve the frequency resolution, windowing functions (see section 3.2.1) are often applied to each time-domain chunk before computing the FFT [29].

2.4 Energy detection

Energy detection is a method used in signal processing to determine the presence of a signal within a noisy background. It has a low computational and implementation complexity and does not need any prior information about the burst signal caused by the pass-by boat event [35]. The idea behind energy detection is to compare the signal energy in a time window to a predefined threshold. If the energy in the window exceeds the threshold, the detector classifies the presence of a boat. If the energy is below the threshold, it is assumed to be only background noise present. The two scenarios, detected signal or no detected signal, can be represented by the following binary assumption:

$$x_n = \begin{cases} b_n + s_n, & \text{detected signal} \\ b_n, & \text{no detected signal} \end{cases}$$

where x_n is the received signal in a time window, b_n is the background noise, and s_n is the burst signal (in this case, the boat) in the index n. When a boat, s_n, is present, the received term, x_n, increases due to the added contribution of the burst signal. In contrast, when only background noise, b_n, is recorded, the energy remains lower. The energy is calculated as the sum of the present energy in the current window, see formula 2.15:

$$E_i = \sum_{n=1}^{N_w} x_n^2 \tag{2.15}$$

where E_i is the signal energy in the i-th window, N_w is the window length, and x_n represents the signal sampled at index n.

To improve event detection robustness, this thesis uses the short-time-average and long-time-average windowing methods (STA/LTA). Initially developed for seismic wave analysis, STA/LTA is adapted here for hydroacoustic event detection. This algorithm was chosen since it is computationally light, robust and proven to work well since it is used since a long time in seismology. The STA reflects the energy of the signal, s_n, and the LTA demonstrates the energy of the background noise, b_n. When the energy rises, the STA increases earlier than the LTA. The shorter STA responds quickly to signal changes, while the longer LTA provides a stable baseline of background noise. Its mathematical representation can be seen for STA in equation 2.16 and for LTA in equation 2.17.

$$STA(t) = \frac{1}{N_{STA}} \sum_{n=t-N_{STA}}^{t} x_n^2 \tag{2.16}$$

$$LTA(t) = \frac{1}{N_{LTA}} \sum_{n=t-N_{LTA}}^{t} x_n^2 \tag{2.17}$$

In these equations, t is a discrete time index (integer), which corresponds to the sample number. N_{STA} and N_{LTA} stand for the number of samples in the short and

long windows, and can be calculated by multiplying the window length in seconds by the sampling frequency. Rather than being predefined, the background noise level is dynamically estimated throughout the recording, allowing it to adapt to changing environmental conditions. The STA/LTA ratio is sensitive to the time of arrival of a burst signal, which is essential for event identification [3, 36].

The detection decision is based on the STA/LTA ratio, R, which is computed using equation 2.18:

$$R(t) = \frac{STA(t)}{LTA(t)} \tag{2.18}$$

If the ratio, R, exceeds the threshold, then a detection is made ($R(t) >$ Threshold), it is non-negative and unbounded above ($R(t) \in [0, \infty]$.
The threshold is a predefined value that impacts the sensitivity and specificity of the energy detector. A small threshold increases the sensitivity but may also detect noise fluctuations as signal bursts. A high threshold reduces false detections but may miss weaker events. The value of the threshold may depend on the chosen recording.

A drawback of the STA/LTA method is that it is sensitive to sudden noise spikes, which can cause false positive detections. Weak signals can go undetected if the ratio is not large enough, so the threshold parameter must be chosen carefully. The length of the STA and LTA windows need to be adapted to the characteristics of the target signal.

For the application in underwater acoustics, if the duration of the signal burst is known, the STA window should be of a similar length to effectively capture the event. Since the duration fluctuates, it is hard to define it. For the LTA, it should be short enough to track variations in background noise, but long enough to avoid being affected too much by signal bursts [36].

2.5 Receiver operating characteristic

The receiver operating characteristic (ROC) curve is a graphical tool to evaluate binary classification systems at various threshold settings. Originally developed during World War II for radar signal detection, the ROC curve has since been adopted in fields such as machine learning, medical diagnostics, finance, and geosciences. It provides information about the relationship between false positive and true positive rates (e.g., detected vs. undetected) [37, 38].

The true positive rate (TPR), also known as sensitivity, is calculated using equation 2.19. It uses the true positives (TP) when a signal burst is correctly detected, and the false negatives (FN) when a signal burst is not detected, but it should have been.

The false positive rate (FPR), also called 1-Specificity (see equation 2.20) uses the false positives (FP) which is when a signal burst is detected but it shouldn't have

been and the true negatives (TN) when no signal was detected and it is correct [39].

A high sensitvity value indicates that most ture positive cases are correct defined, with a few false negatives. However this does not mean that all detections are correct, it reflects the proportional of actual events that were successfully detected. If there are no false positives but all true negatives are detected, it results in a high Specificity (see equation 2.21). Then one can be sure that it is right if it says there is no detection.

The ROC curve represents the relationship between detection sensitivity and the likelihood of false alarms (specificity). Reducing the detection threshold increases sensitivity, leading to more true positives but also more false positives. Raising the threshold enhances specificity at the cost of potentially missing true positives [4].

$$TPR = \frac{\text{True Positivies (TP)}}{\text{True Positives (TP) + False Negatives (FN)}} \tag{2.19}$$

$$FPR = \frac{\text{False Positivies (FP)}}{\text{False Positives (FP) + True Negatives (TN)}} \tag{2.20}$$

$$Specificity = \frac{\text{TN}}{\text{TN+FP}} \tag{2.21}$$

For the ROC curves, the TPR (y-axis) is plotted against the FPR (x-axis). The further the line is to the upper left corner with coordinates (x = 0, y = 1), the higher the sensitivity (no false negatives) and also the specificity (no false positives). This upper left corner represents an ideal classification. The perfect curve would have a 100 % sensitivity (no false negatives) and specificity (no false positives). The diagonal line from coordinates (x = 0, y = 0) to (x = 1, y = 1) is a reference line. The closer the curve is to this line, the less accurate the detection. An example plot for a perfect ROC curve can be seen in Figure 2.6.

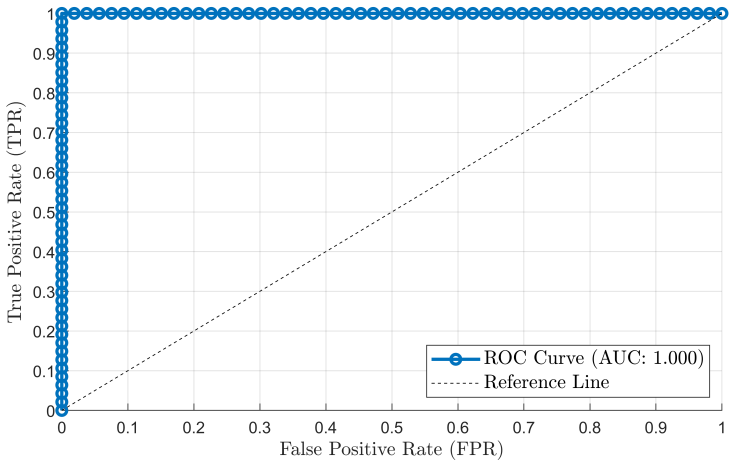

Figure 2.6: Example of a perfect ROC curve.

The Area Under the Curve (AUC) quantifies the ability to distinguish between positive and negative classes, serving as a measure of separability. The higher the AUC, the better the model is at correctly detecting recognized events [40]. An AUC close to 1 demonstrates excellent specificity between classes. In contrast, an AUC near 0 indicates poor classification performance, where predictions are systematically incorrect. An AUC of 0.5 suggests no discrimination capability, equivalent to random guessing. The AUC is calculated using equation 2.22, which estimates the area under the curve using trapezoidal integration [41].

$$AUC = \sum_{i=1}^{n-1} (FPR_{i+1} - FPR_i) \cdot \frac{TPR_{i+1} + TPR_i}{2} \tag{2.22}$$

3
Methods

This chapter describes the methodology used to develop an effective detection algorithm. It starts with an overview of the data collection process, followed by an explanation of the key parameters that can be adjusted in the algorithm.

3.1 Measurements

The measurements were carried out by the Acoustics Team at IVL. These continuous measurements were made near Koster in western Sweden in August 2024. Koster was selected as a study site due to its acoustic environment, featuring high-traffic and low-traffic areas in deeper and shallower water.
Hydrophones could be placed at heavily used boating routes as well as in very shallow water, with traffic emerging seldom. The locations chosen from 1 to 5 can be seen in Figure 3.1. This map is © OpenStreetMap contributors and is licensed under the Open Database License (ODbL).

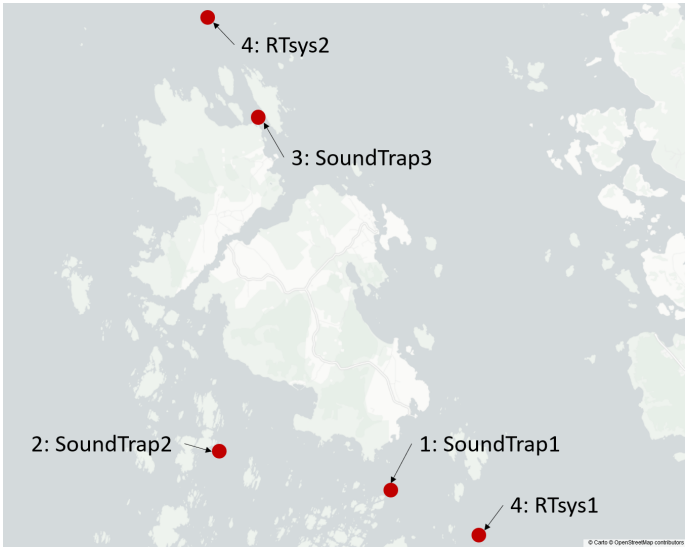

Figure 3.1: Measurement positions from 1 to 5. Source: © OpenStreetMap contributors.

The hydrophone types used are: "SoundTrap 300 LF" by Ocean Instruments, which recorded at 96 kHz and 16 bit, and "RTsys Sylence LP" by the company RTSYS, which recorded at 128 kHz and 24 bit. The distribution of these on the locations

can be seen in Table 3.1. An example of the hydrophones used in generating the data is shown in Figure 3.2.

Table 3.1: The location numbers with the corresponding hydrophone Model and ID, their coordinates, and deployment depth in meters.

Location Nr	Hydrophone Model & ID	Geographical Coordinates	Deployment Depth (m)
1	SoundTrap1	58° 51.459'N 11° 3.131'E	18 m
2	SoundTrap2	58° 51.771'N 11° 0.321'E	10 m
3	SoundTrap3	58° 54.546'N 11° 0.985'E	7 m
4	RTsys1	58° 51.065'N 11° 4.569'E	22 m
5	RTsys2	58° 55.414'N 11° 0.154'E	28 m

Figure 3.2: Example of the used hydrophones, left SoundTrap and right RTsys.

For the evaluation of the ED, not all measurement positions were used. SoundTrap 2 and 3, as well as RTsys 1, were sometimes corrupted by mechanical disturbance noises. So the data from these was disregarded.

3.1.1 Recordings

The recordings of SoundTrap 2 were saved for a length of 179 minutes, and the recordings of RTsys 1 for 43 minutes. For the evaluation of the parameters bandpass frequencies and window lengths of STA and LTA, six of the SoundTrap recordings were used, and six of the RTsys recordings. This resulted in 12 recordings in total, with a total amount of 22 hours and 20 minutes. These included 85 passing events of boats.

To establish a ground truth for the evaluation, all recordings were manually reviewed. Each boat passage was identified and annotated by listening to the data and inspecting the corresponding spectrograms.

3.2 Energy Detector

The energy detector (ED) identifies signal bursts based on energy variations in selected frequency bands. It consists of three main components: a bandpass filter to isolate relevant frequency ranges, a windowing function to analyze time segments, and a threshold to distinguish signal bursts from background noise. For the implementation of the ED, MATLAB was used. Unless otherwise stated, all detection results presented in this work were obtained using the broadband energy detection method. The multiband energy detection approach (described in section 3.3) was implemented at a later stage of the project to investigate potential performance improvements. The following sections describe the selection and evaluation of these components.

3.2.1 Window

The Blackman-Harris window was used to window the signal. Due to high spectral side lobes, a rectangular window is not considered acceptable for robust spectrum analysis. The Blackman-Harris window has very small side lobes with the trade-off of a wide main lobe and is recommended for high-precision frequency analysis applications.
Looking at the STA/LTA algorithm, in seismic usages, the length of the shorter window (STA) is picked to resemble the length of the duration of the signal burst. The long window (LTA) is chosen to represent multiple periods of the signal burst. Keeping this in mind, different STA and LTA times were chosen. For the STA, 1 minute to 4 minutes was used, for the LTA, 10 minutes to 200 minutes. Here, the STA represents the possible durations of signal bursts of the recordings. Every short window was tested with every long window.

3.2.2 Bandpass

The bandpass filter focuses on the primary spectrum where boat noise is present. ROC curves evaluate the performance of different lower and upper limits for the bandpass filter.
The range was divided after Table 3.2 to evaluate different frequency bands. These were chosen to analyze a good distribution over the given range and predict trends more easily. The used filter is a Butterworth filter due to its flat frequency response in the passband.

3.2.3 Threshold

The threshold needs to be picked depending on the goals of the detection process. The lower the set threshold, the more sensitive the ED is to signal bursts. The higher the threshold, the higher the specificity.

Table 3.2: The used frequency ranges for the evaluation of the bandpass.

Lower Limit	Upper Limit
30 Hz	250 Hz
250 Hz	1000 Hz
1000 Hz	4000 Hz
4000 Hz	20000 Hz

In this context, the threshold refers to the STA/LTA energy raio $R(t)$ (see Equation 2.18). If the ratio is bigger than the set threshold an event is classified as a boat passage. A threshold of 1 indicates that the energy in the STA window equals the energy in the LTA window, values below 1 allow the detection of events with lower energy relative to background noise.

The threshold range used to estimate the ROC curves for the parameter's window length and bandpass frequencies was logarithmically spaced from 0.01 to 100, with a manually added 0, resulting in 101 points on the array. The logarithmic threshold range was selected to ensure sensitivity at low and high threshold values, capturing a wide range of signal intensities for the ROC curve estimation.

To estimate a good threshold range for the energy detector, the lower boundary and the upper boundary have to be estimated. Since a value of 0 for the threshold would mean that every STA window would be counted as a positive detection the lower boundary was set to 0.1. To find the upper boundary, the threshold was raised in 0.1 steps until no false detection occurred. The recordings were expanded by five, resulting in 17 recordings used for the estimation of missed and false detections.

3.3 Multiband

To enhance detection robustness and maintain computational efficiency, a multiband ED approach was developed as a refinement of the original broadband ED. The broadband detector used a single bandpass filter to isolate vessel noise within a frequency range. While this approach performed well, it treated the entire band as a whole, potentially overlooking more detailed spectral patterns that vary across subbands.

In the broadband ED, the signal is first filtered using a Butterworth bandpass filter to isolate the desired frequency range. Following this, the signal is processed using the STA/LTA algorithm to identify potential events based on the generated ratio compared to a predefined threshold.

In contrast, the multiband ED introduces additional frequency resolution. For each STA window, the signal is first divided into 50% overlapping one-second segments using a Blackman-Harris window to reduce spectral leakage. An FFT is then applied

to each of these segments, yielding its frequency-domain representation. Within the target frequency range, the spectrum is further divided into multiple narrow subbands, and the energy within each subband is computed.

This results in a matrix where each row corresponds to an STA window and each column to a specific frequency band, capturing the energy distribution over time and frequency. The LTA is constructed using the STA windows, producing a matrix of the same shape.

The STA and LTA matrices are then divided element-wise to calculate the STA/LTA energy ratio for each of the subbands. From the resulting ratio matrix, the maximum ratio value across all frequency bands is chosen to represent the STA/LTA score for that time step. This peak value is then compared against a predefined detection threshold. If it exceeds the threshold, an event is marked as detected.

This multiband formulation allows for better sensitivity to localized spectral energy changes, improving the reliability of detections in noisy or complex acoustic environments.

Since the ED counts the number of detected STA windows, neighbouring detected windows were grouped into one detection. This was done for signals with a duration of more than the length of the STA window.

For the multiband vs. broadband comparison presented in Section 4.4 the LTA window length is not fixed across recordings. Instead, it was dynamically adjusted to match the length of each recording. Previous evaluations had a fixed LTA duration. As a result, slight differences in AUC values for the broadband method may occur due to this variation in LTA configuration.

4

Results

This chapter presents the results of the energy detection parameter evaluation. The estimated AUC values for all combinations of STA, LTA, and Bandpass settings are provided in Table A.1 in the Annex. Corresponding ROC curves are shown in Figures A.1 to A.80.

4.1 Window

The optimal STA window length was found to be 3 minutes, achieving a mean AUC of 0.858. The 2 minute STA also performed well (mean AUC = 0.845) but showed slightly less consistency across different configurations, also not achieving peak values. The 1 minute STA had a lower mean AUC of 0.835, while the 4 minute STA performed the worst (mean AUC = 0.790). The maximum, minimum, and mean values of the AUC per STA length can be seen in Table 4.1.

These results are based on evaluation across all tested combinations of LTA window length and bandpass frequency ranges. The minimum, maximum, and mean AUC values per STA length are summarized in Table 4.1. Figure 4.1 shows the different performances for the four different STA lengths at a fixed LTA length of 170 minutes at bandpass 250 Hz - 1000 Hz. The points on the curve are for different thresholds (the ratio from STA/LTA, R) in logarithmic spacing from 0.01 to 100 with a 0 added manually, for each threshold point the TPR and FPR is calculated.

Table 4.1: The STA in minutes, values represent the minimum, maximum, and mean AUC across all evaluated combinations of LTA window lengths and bandpass frequency ranges.

STA (min)	Min AUC	Max AUC	Mean AUC
1	0.713	0.880	0.835
2	0.699	0.901	0.845
3	0.684	0.912	0.858
4	0.702	0.838	0.790

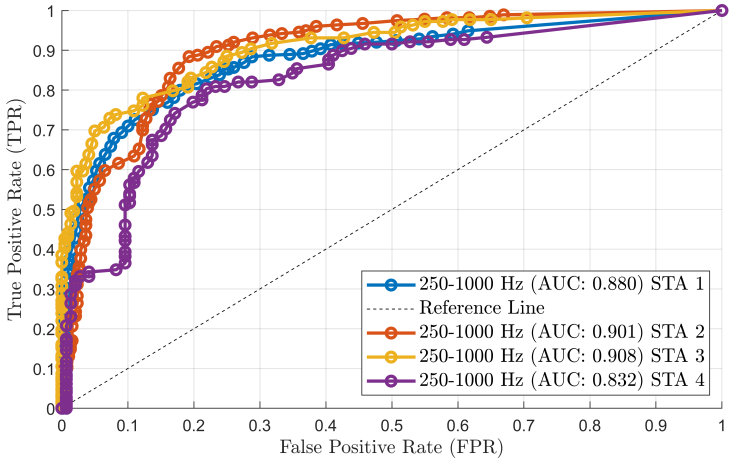

Figure 4.1: Performance of the STA lengths 1 minute to 4 minutes for a fixed LTA length of 170 minutes at bandpass 250 Hz - 1000 Hz.

For the LTA window, performance generally improved with increasing LTA length. The best results were obtained at 170 minutes, achieving a mean AUC of 0.850. Two plateaus in the AUC values were obtained, first at 30 and 40 minutes and second at 160 and 170 minutes. The highest increase in performance was from increasing the LTA from 10 minutes to 30 minutes. After 190 minutes, the performance dropped. The LTA of 10 minutes had the lowest AUC values overall. The LTA time in minutes with their corresponding minimum, maximum, and mean AUC can be seen in Table 4.2. These results are calculated across all evaluated combinations of STA window length and bandpass frequency ranges for each LTA length.

Table 4.2: The LTA in minutes, values represent the minimum, maximum, and mean AUC across all tested sTA window length and bandpass frequency configurations.

LTA (min)	Min AUC	Max AUC	Mean AUC
10	0.684	0.766	0.725
20	0.737	0.843	0.799
30	0.749	0.871	0.822
40	0.758	0.879	0.823
50	0.765	0.885	0.831
60	0.758	0.892	0.834
70	0.762	0.891	0.837
80	0.756	0.897	0.840
90	0.758	0.897	0.840
100	0.755	0.898	0.837
110	0.756	0.902	0.839
120	0.755	0.902	0.840
130	0.759	0.905	0.839
140	0.776	0.908	0.846
150	0.775	0.910	0.848
160	0.775	0.912	0.848
170	0.782	0.912	0.850
180	0.779	0.910	0.849
190	0.770	0.911	0.848
200	0.763	0.909	0.846

The results indicate that an LTA of 170 minutes achieves a strong performance. Beyond this point, increasing the LTA further provides no benefits in AUC. The ROC curves for the combination of STA 3 minutes and LTA 10 minutes, 40 minutes, 170 minutes, and 200 minutes can be seen in Figure 4.2.

4.2 Bandpass

The choice of bandpass filter significantly influenced detection performance. The best-performing frequency band was 250 Hz - 1000 Hz (mean AUC = 0.862), followed closely by 1000 Hz - 4000 Hz (mean AUC = 0.848). The high-frequency band had the lowest performance (4000 Hz - 20000 Hz, mean AUC = 0.803). The maximum, minimum, and mean AUC values can be seen in Table 4.3. These results were computed across all tested combinations of STA and LTA window lengths for each frequency band.

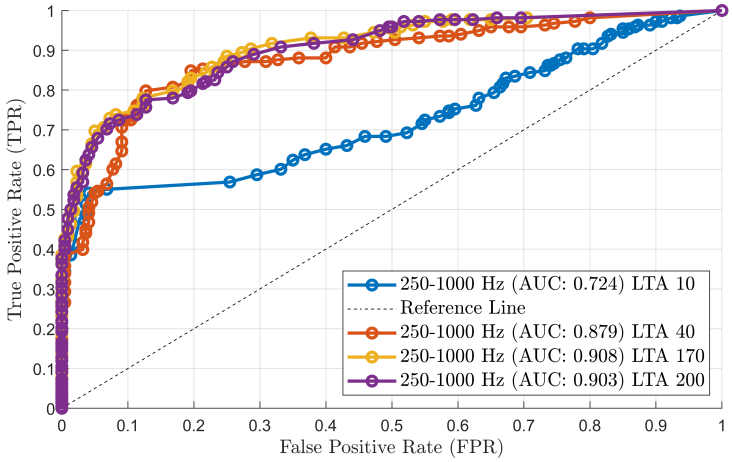

Figure 4.2: Performance of the LTA lengths 10 minutes, 40 minutes, 170 minutes, and 200 minutes for a fixed STA length of 3 minutes at bandpass 250 Hz - 1000 Hz.

Table 4.3: The Bandpass in Hz, values representing the minimum, maximum, and mean AUC across all evaluated STA and LTA configurations.

Lower Limit (Hz)	Upper Limit (Hz)	Min AUC	Max AUC	Mean AUC
30	250	0.705	0.862	0.816
250	1000	0.724	0.908	0.862
1000	4000	0.723	0.912	0.848
4000	20000	0.684	0.844	0.803

The four original tested frequency ranges for an STA of 3 minutes and an LTA of 170 minutes can be seen in figure 4.3.

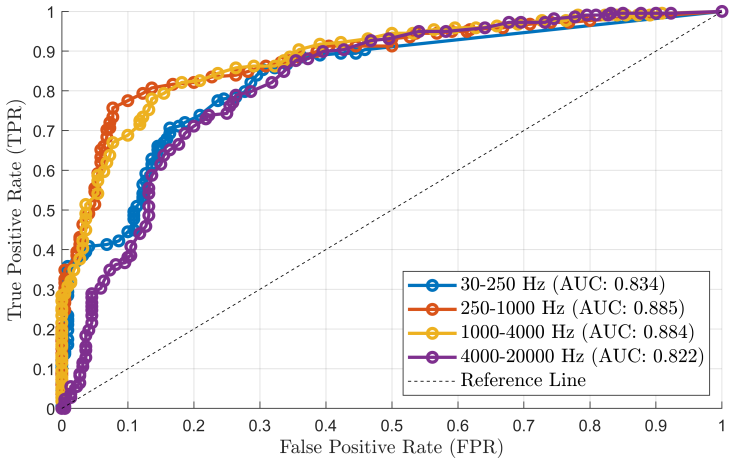

Figure 4.3: The ROC curve for STA of 3 minutes and LTA of 170 minutes.

Since the best performing bands are 250 Hz to 1000 Hz and 1000 Hz to 4000 Hz, this frequency range was further evaluated. The highest achieved AUC value is the

Band from 100 Hz to 4000 Hz with an AUC of 0.930 (see figure 4.4).

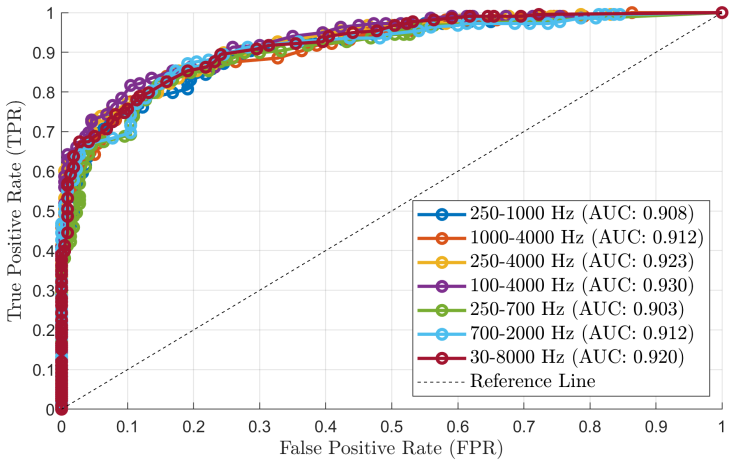

Figure 4.4: The ROC curve for STA of 3 minutes and LTA of 170 minutes with different bandpass filters.

4.3 Threshold

The trade-off between FPR and TPR was considered for selecting the threshold. For the combination of STA 3 minutes, LTA as the recording length, and 100 Hz to 4000 Hz, choosing a FPR of approximately 0.1, the TPR is at almost 0.8 (see figure 4.3). For this combination, all recordings were tested, and the values of TPR, FPR, and threshold were noted (see table 4.4).

Table 4.4: The TPR and FPR with their corresponding Threshold value per recording.

Recording Nr.	TPR	FPR	Threshold
1	0.8286	0.1250	0.0933
2	0.9474	0.0952	0.0443
3	0.6471	0.0952	0.1789
4	0.9615	0.0909	0.0278
5	0.8649	0.0909	0.0254
6	0.8750	0.1111	0.0774
7	1	0	0.3126
8	0.6667	0.1250	0.1963
9	1	0	0.1024
10	1	0.1111	0.0443
11	1	0.0909	0.2595
12	1	0	0.2848

This resulted in a mean value for TPR of 0.9, FPR of 0.1, and threshold of 0.1. A value of 0.1 was picked as the lower limit for testing the threshold range. Table 4.5

presents the number of missed boat detections across different threshold values for each recording. The color scale visually represents the severity of missed detections, with green indicating no misses, yellow indicating one, and increasingly darker red tones representing higher counts. By identifying the threshold at which the first missed detection occurs for each recording, a mean threshold value of 0.5 is obtained.

Table 4.5: Number of missed boat detections across thresholds (0.1 to 1.3). Colors indicate severity (green = none, red = worse).

Rec Nr.	0.1	0.2	0.3	0.4	0.5	0.6	0.7	0.8	0.9	1.0	1.1	1.2	1.3
1	0	0	1	1	1	2	2	2	2	2	2	2	2
2	0	0	0	0	1	2	2	3	3	3	4	4	4
3	0	0	0	0	0	0	0	1	2	3	3	3	3
4	0	0	0	0	1	1	2	3	3	3	4	4	4
5	0	0	1	2	2	3	3	3	3	6	6	6	6
6	0	0	0	0	0	1	1	1	1	2	2	2	2
7	0	0	0	0	1	1	1	1	1	1	1	1	1
8	0	0	0	1	1	1	1	1	1	1	1	1	1
9	0	0	0	0	0	0	0	0	0	0	0	1	1
10	0	0	0	0	0	0	0	0	0	0	0	0	0
11	0	0	0	0	0	0	0	0	0	0	0	0	0
12	0	0	0	1	1	1	1	1	1	1	1	1	1
13	0	0	1	1	1	1	1	1	1	2	2	2	2
14	0	0	0	0	0	0	0	0	0	0	0	0	0
15	0	0	0	0	0	0	0	0	0	0	0	0	0
16	0	0	0	2	2	2	2	2	2	2	2	2	2
17	0	0	0	0	0	0	0	0	0	0	0	0	0

To estimate the upper threshold boundary, the number of false detections was analyzed similarly to the missed detections. Each recording was evaluated across the range of threshold values until no false detections remained. Table 4.6 summarizes the number of false detections per recording for each threshold. By identifying the threshold at which false detections ceased, a mean threshold value of 0.8 was determined.

Table 4.6: Number of false boat detections across thresholds (0.1 to 1.3). Colors indicate severity (green = none, red = worse).

Rec Nr.	0.1	0.2	0.3	0.4	0.5	0.6	0.7	0.8	0.9	1.0	1.1	1.2	1.3
1	0	0	0	0	0	0	0	0	0	0	0	0	0
2	0	0	0	0	0	0	0	0	0	0	0	0	0
3	0	0	0	0	0	0	0	0	0	0	0	0	0
4	1	1	1	0	0	0	0	0	0	0	0	0	0
5	0	0	0	0	0	0	0	0	0	0	0	0	0
6	0	0	0	0	0	0	0	0	0	0	0	0	0
7	0	0	0	0	0	0	0	0	0	0	0	0	0
8	0	0	0	0	0	0	0	0	0	0	0	0	0
9	0	0	0	0	0	0	0	0	0	0	0	0	0
10	0	0	0	0	0	0	0	0	0	0	0	0	0
11	1	1	1	1	1	1	1	1	1	1	1	1	0
12	0	0	0	0	0	0	0	0	0	0	0	0	0
13	0	0	0	0	0	0	0	0	0	0	0	0	0
14	0	0	0	0	0	0	0	0	0	0	0	0	0
15	0	0	0	0	0	0	0	0	0	0	0	0	0
16	1	1	1	1	1	1	0	0	0	0	0	0	0
17	0	0	0	0	0	0	0	0	0	0	0	0	0

4.4 Multiband

To evaluate whether the multiband formulation offers an improvement over the originally used broadband energy detection, a comparison was performed. This comparison, shown in Figure 4.5, demonstrates that the multiband ED yields a higher AUC value, suggesting improved detection performance across all tested frequency ranges.

Specifically, in the broadband implementation, AUC scores of 0.909, 0.912, and 0.933 were achieved for the frequency bands 250 Hz to 1000 Hz, 1000 Hz to 4000 Hz, and 100 Hz to 4000 Hz. In contrast, the multiband approach improved upon these results with AUC scores of 0.936, 0.939, and 0.949 for the same frequency bands. These results highlight the benefit of incorporating finer spectral resolution into the energy detection process. Interestingly, for both the 250 Hz to 1000 Hz and 1000 Hz to 4000 Hz bands, the AUC increased by exactly 0.027, suggesting that the multiband formulation provided a consistent performance gain across these ranges. The increase in the full-band range (100 Hz to 4000 Hz) was slightly smaller, potentially due to overlapping frequency information. At an FPR lower than 0.07, the Broadband Detector performs better than the Multiband. Above the FPR of 0.07, the Multiband Detector performs better.

Note that in this comparison, the LTA window was scaled to the duration of each recording, which may account for minor differences in broadband AUC values compared to earlier results where a fixed LTA length was used.

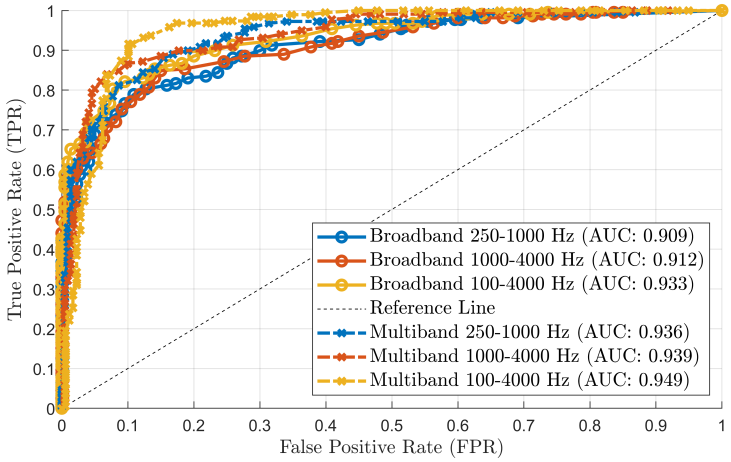

Figure 4.5: Comparison of the Broadband Energy Detector and the Multiband Energy Detector as ROC curve with AUC values.

5
Discussion

Due to mechanical noise contamination, some hydrophone recordings were excluded from the evaluation. This noise would bias the ED by artificially introducing high energies and therefore increasing the background noise level, masking quieter boats, potentially affecting detection sensitivity. Evaluation of ED parameters using a larger dataset with additional hydrophone data would improve robustness. However, the computational cost was a limiting factor.

The dataset consisted of 12 recordings from two hydrophones, with six recordings lasting 42 minutes and six lasting 3 hours. While this ensured a balanced dataset, having a larger variety of recording lengths and more hydrophones could enhance statistical reliability and generalizability.

The evaluation showed that the LTA length affects the detection performance. When an LTA shorter than the full recording is used it introduces inconsistencies, setting the LTA to cover the whole recording provides a stable and representative baseline. It ensures comparable STA/LTA ratios across the recording.
This approach connects the LTA length to the file length, which is practical for offline analysis but impractical for real-time detection where noise conditions fluctuate. In such cases, an LTA of fixed or adaptive length would be preferred. Father study would be needed to define these optimal LTA lengths for real-time detection.
The results obtained for the STA window duration are reasonable and match with information found in related domains, such as seismology, where the STA/LTA algorithm is used. The STA duration is often chosen to match the typical duration of the signal of interest. In this thesis, the most effective STA durations were 2 and 3 minutes, which correspond to the average duration of vessel passages present in the recordings. This points to the window lengths being sufficient to capture the transient energy associated with boat events without being overly influenced by the surrounding background noise.

An array of binary values (0 and 1) was manually written for ED evaluation to indicate if STA windows contain a detection. Since a single person performed this annotation process, there is potential for subjectivity and bias in determining a detection. A more reliable approach would involve multiple people annotating, followed by a method (e.g., majority voting) to reduce individual biases and improve annotation accuracy.

The frequency band selection also had meaningful results. The best-performing

bands excluded very low frequencies, where background noise dominates. Bands such as 250 Hz to 1000 Hz and 1000 Hz to 4000 Hz were particularly effective, indicating that important energy from boat passages is concentrated above 250 Hz and below 4000 Hz, but the best band is from 100 Hz to 4000 Hz. These findings are consistent with the acoustic signature of boats, which typically includes dominant components in the low- to mid-frequency ranges. The results suggest that excluding the lowest frequency range can improve detection performance by reducing interference from non-relevant low-frequency background noise.

The relatively low threshold values observed in this thesis are consistent with expectations for underwater acoustic environments, where noise levels can vary significantly and signals of interest, such as boat noises, may often be subtle. Since energy detection is sensitive to small variations in signal energy, a lower threshold ensures that quieter or distant boat sounds are still detected. At the same time, excessively low thresholds increase the risk of detecting background noise or non-relevant events, explaining the rise in false positives.

Higher thresholds, while reducing false detections, may miss valid but low-amplitude signals. Therefore, the derived threshold range (0.1 to 1.3) with an effective working window between 0.5 and 0.8 reflects a good compromise. This range accommodates both the variability of real-world acoustic conditions and the limitations of a simple energy detection algorithm.

The improvement in AUC values when using the multiband ED suggests that a more detailed spectral resolution can enhance the sensitivity of the detection process. By analyzing energy distributions across smaller frequency subbands, the multiband approach is likely better able to capture subtle spectral characteristics associated with relevant events. This appears particularly beneficial in complex acoustic environments where energy may not be concentrated in a single broad frequency range. Future work could explore adaptive frequency band selection or weighting strategies to optimize the multiband formulation further.

Interestingly, the AUC values generated during the multiband vs. broadband comparison were slightly higher than those from earlier evaluations using a fixed LTA window. This improvement appears to stem from matching the LTA length to the duration of each individual recording. This observation shows the importance of tailoring the LTA configuration to the specific length of the recording, as it can lead to more accurate long-term energy estimation and improve detection performance.

Another interesting observation is the performance at an FPR below 0.07. The broadband detector outperforms the multiband approach, above a FPR of 0.07, the multiband detector performs better.

This could be due to the broadband detector benefiting from the broader frequency spectrum as it integrates the energy across that area. This makes it effective at capturing the high-energy signals, as it sums the power from all relevant frequencies,

increasing the signal-to-noise ratio. The multiband detector, on the other hand, divides the energy across several frequency bands, which can dilute the overall signal strength. Therefore it is better for tonal signal detection.

As the FPR increases and the detection becomes more sensitive, the multiband detector begins to outperform due to its frequency discrimination. The evaluation of energy in specific bands can help to distinguish boat-related signals from background noise. This can be helpful in situations with e.g. rain as background noise, since the band representing this noise can be ignored.

6
Conclusion

This thesis developed and evaluated an automated energy detector (ED) for identifying recreational boats in underwater recordings. The system is based on the Short-Time Average / Long-Time Average (STA/LTA) algorithm, a technique used in seismology for detecting signal bursts. The goal was do adapt and optimize this method for marine environments, where background noise varies and boat signatures differ from each other.

To achieve this, the system was tested on real underwater recordings collected during fieldwork along the Swedish coastline. Several key parameters influencing detection performance were evaluated: the length of the STA and LTA windows, the choice of bandpass filter frequency ranges, and the detection threshold. Receiver Operating Characteristic (ROC) curves were generated, and the Area Under the Curve (AUC) value was used as the metric for assessing results. Additionally, a multiband variation of the ED was implemented to see if spectral resolution improves the performance in comparison with a broadband ED.

6.1 Time Window

The results indicate that an STA of 3 minutes consistently achieves the highest AUC values across different frequency bands. While an STA of 2 minutes is competitive, it does not reach the same peak performance. The 1 minute STA performs moderately well but lacks consistency. Conversely, an STA of 4 minutes leads to a noticeable performance drop, suggesting that excessively long STA windows reduce sensitivity to transient acoustic events.

For the LTA window, performance steadily improves with increasing duration, reaching its peak at 170 minutes. A plateau in the AUC values can be seen at 30 and 40 minutes LTA, as well as at 160 and 170 minutes LTA. This could be due to the length of the recordings. Six of the twelve recordings are 43 minutes long and the other six are 179 minutes long. This indicates that the LTA duration has to be the same as the length of the recording.

The best-performing configuration is an STA of 3 minutes and an LTA of 170 minutes, achieving high AUC. The ROC curve for this configuration can be seen in Figure 4.3.

6.2 Bandpass

The best performing frequency band is 250 Hz to 1000 Hz, achieving an AUC of 0.885 for the optimal STA/LTA configuration. At an FPR of 0.1, the TPR is nearly 0.8, indicating that 80 % of vessels are correctly detected, while 10 % of detections are false alarms.

When looking into the closer evaluation for the bandpass frequencies, a broader range (100 Hz to 4000 Hz) has a higher AUC value as well as a better performance. The point of an FPR at 0.1 shows that the performance of a broader band achieves higher values for the TPR. Concluding from this, the band 100 Hz to 4000 Hz is seen as the best performing band.

The 1000 Hz to 4000 Hz band also performed well, but slightly worse than the 250 Hz to 1000 Hz band, suggesting that the most relevant vessel noise components lie in the lower frequency range. The poorest performance was observed in the 4000 Hz to 20000 Hz band, likely due to high-frequency attenuation and reduced vessel noise contribution in this range.

6.3 Threshold

The threshold value refers to the STA/LTA energy ratio, above which a event is counted as positive detection. A value of 1 indicates the short-term energy equals the long-term average energy. Values below 1 allow the detection of events with lower energy relative to background noise. If recordings with many boat passages present are used, the STA energy sometimes can't even exceed the LTA energy. The threshold values in this thesis were evaluated using recordings with multiple boats present.

The evaluation of missed and falsely detected boats across various thresholds suggests that the range between 0.1 and 1.3 is suitable for detecting boats in underwater recordings. Within this, thresholds below 0.5 result in a low probability of missing actual events, while thresholds above 0.8 significantly reduce the risk of false detections. Based on the analysis, the optimal threshold for reliable detection lies between 0.5 and 0.8, where a balance between sensitivity and specificity is achieved.

6.4 Multiband

The introduction of a multiband energy detection approach gave consistently higher AUC values compared to the previously used broadband method. The Multiband ED outperformed the Broadband ED above an FPR of 0.07. This indicates that a finer spectral resolution contributes to improved detection performance depending on the threshold. The multiband formulation, therefore, represents a promising

refinement for enhancing the energy-based detection, especially in acoustically complex situations. The results also indicate that adapting the LTA length to the recording duration can yield slightly improved detection performance. This highlights the value of aligning the LTA duration with the length of the recording.

6.5 Future work

An alternative approach to building the ED could have been to utilize Machine Learning or Artificial Intelligence. These techniques have shown great promise in various applications, offering the potential to improve the detection accuracy by learning complex patterns from data. For this, a significantly larger dataset would have been required to train and validate a robust model. Also, the selection of appropriate features, model architecture, and training methodology would have introduced further complexity to the development. While Machine Learning and Artificial Intelligence could enhance detection performance, the trade-off between computational efficiency, data availability, and model interpretability should be carefully considered in future work.

One limitation of the current ED is the binary nature of the output, each signal is classified as a detection or not. However, underwater acoustic environments are often complex and noisy, making such binary decisions potentially sensitive to threshold settings and signal variability. A promising direction for future work could be to develop a probabilistic extension of the energy detector, where the output reflects the likelihood that a signal corresponds to a boat event.

Instead of providing a simple yes or no output, the ED could return a probability value (e.g., "there is a 70 % chance this signal is a boat"), offering a more informative interpretation. This would allow for more flexible decision-making, such as incorporating uncertainty into tracking algorithms or adjusting sensitivity dynamically based on contextual data (e.g., time of day, known traffic patterns). Such an approach could also support a more transparent evaluation of detection, improving the usability and robustness of the system in real-world scenarios.

The findings of this thesis align with the potential improvements outlined in the abstract. The probabilistic extension to the energy detector, where the outcome is expressed as likelihood and not as binary decision, is a promising direction for enhancing robustness. Similar, the adaptation of LTA length and bandpass selection to real-time changes could improve the detector's applicability for real-time underwater monitoring. These future developments would address the limitations identified in this thesis and further increase the detector's performance.

Bibliography

[1] P.-O. Moksnes, L. Eriander, J. Hansen, J. Albertsson, M. Andersson, U. Bergström, J. Carlström, J. Egardt, R. Fredriksson, L. Granhag, F. Lindgren, K. Nordberg, I. Wendt, S. Wikström, and E. Ytreberg, "Fritidsbåtars på verkan på grunda kustekosystem i sverige (*the impact of recreational boating on shallow water, coastal ecosystems in sweden*)," Tech. Rep. 2019:3, Havsmiljö, 2019.

[2] A. T. Johansson, E. Lalander, A.-S. Krång, and M. H. Andersson, "Speed dependence, sources, and directivity of small vessel underwater noise," *The Journal of the Acoustical Society of America*, vol. 156, no. 4, pp. 2077–2087, 2024.

[3] Z. Chen, H. Liu, J. Zhao, and T. Bi, "Real-time event detection based on sta/lta method using field synchrophasor measurements," *IEEE Transactions on Power Delivery*, 2023.

[4] J. V. Carter, J. Pan, S. N. Rai, and S. Galandiuk, "Roc-ing along: Evaluation and interpretation of receiver operating characteristic curves," *Surgery*, vol. 159, no. 6, pp. 1638–1645, 2016.

[5] S. Matzner, A. Maxwell, J. Myers, K. Caviggia, J. Elster, M. Foleyy, M. Jones, G. Ogdenz, E. Sorensenz, L. Zurkz, *et al.*, "Small vessel contribution to underwater noise," in *OCEANS 2010 MTS/IEEE SEATTLE*, pp. 1–7, IEEE, 2010.

[6] G. Haviland-Howell, A. S. Frankel, C. M. Powell, A. Bocconcelli, R. L. Herman, and L. S. Sayigh, "Recreational boating traffic: a chronic source of anthropogenic noise in the wilmington, north carolina intracoastal waterway," *The Journal of the Acoustical Society of America*, vol. 122, no. 1, pp. 151–160, 2007.

[7] J. A. Hildebrand, "Anthropogenic and natural sources of ambient noise in the ocean," *Marine Ecology Progress Series*, vol. 395, pp. 5–20, 2009.

[8] C. Erbe, S. A. Marley, R. P. Schoeman, J. N. Smith, L. E. Trigg, and C. B. Embling, "The effects of ship noise on marine mammals—a review," *Frontiers in Marine Science*, vol. 6, p. 606, 2019.

[9] D. A. Abraham, *Underwater acoustic signal processing: modeling, detection, and estimation*. Springer, 2019.

[10] T. Rossing, *Springer handbook of acoustics*. Springer Science & Business Media, 2007.

[11] Y. Kularia, S. Kohli, and P. P. Bhattacharya, "Analyzing propagation delay, transmission loss and signal to noise ratio in acoustic channel for underwater wireless sensor networks," in *2016 IEEE 1st international conference on power electronics, intelligent control and energy systems (ICPEICES)*, pp. 1–5, IEEE, 2016.

[12] J. A. L. Sirvent, "Realistic acoustic prediction models to efficiently design higher layer protocols in underwater wireless sensor networks," *Diss. universidad miguel hernandez de elche*, 2012.

[13] F. B. Jensen, W. A. Kuperman, M. B. Porter, H. Schmidt, F. B. Jensen, W. A. Kuperman, M. B. Porter, and H. Schmidt, "Fundamentals of ocean acoustics," *Computational ocean acoustics*, pp. 1–64, 2011.

[14] F. Fahy and D. Thompson, *Fundamentals of sound and vibration*. CRC press, 2015.

[15] R. F. Coates and R. Coates, *Underwater acoustic systems*. Springer, 1990.

[16] L. Possenti, L. de Nooijer, C. de Jong, F.-P. Lam, S. Beelen, J. Bosschers, T. van Terwisga, R. Stigter, and G.-J. Reichart, "The present and future contribution of ships to the underwater soundscape," *Frontiers in Marine Science*, vol. 11, p. 1252901, 2024.

[17] C. M. Duarte, L. Chapuis, S. P. Collin, D. P. Costa, R. P. Devassy, V. M. Eguiluz, C. Erbe, T. A. Gordon, B. S. Halpern, H. R. Harding, *et al.*, "The soundscape of the anthropocene ocean," *Science*, vol. 371, no. 6529, p. eaba4658, 2021.

[18] J. Hildebrand, "Sources of anthropogenic sound in the marine environment," in *Report to the policy on sound and marine mammals: an international workshop. US Marine Mammal Commission and Joint Nature Conservation Committee, UK. London, England*, 2004.

[19] H.-j. Ju and J.-s. Choi, "Experimental study of cavitation damage to marine propellers based on the rotational speed in the coastal waters," *Machines*, vol. 10, no. 9, p. 793, 2022.

[20] T. Johansson, C. Andersson, A.-S. Krång, and C. Andersson, "Underwater noise from fairways–policies, incentives and measures to reduce the environmental impact," 2023.

[21] D. K. Wittekind, "A simple model for the underwater noise source level of ships.," *Journal of Ship Production & Design*, vol. 30, no. 1, 2014.

[22] K. Abrahamsen, "The ship as an underwater noise source," in *Proceedings of Meetings on Acoustics*, vol. 17, AIP Publishing, 2012.

[23] M. Parsons and M. Meekan, "Acoustic characteristics of small research vessels," *Journal of Marine Science and Engineering*, vol. 8, no. 12, p. 970, 2020.

[24] G. M. Wenz, "Acoustic ambient noise in the ocean: spectra and sources," *The journal of the acoustical society of America*, vol. 34, no. 12, pp. 1936–1956, 1962.

[25] P. H. Dahl, J. H. Miller, D. H. Cato, and R. K. Andrew, "Underwater ambient noise," *Acoustics Today*, vol. 3, no. 1, pp. 23–33, 2007.

[26] M. L. Banner and D. H. Cato, "Physical mechanisms of noise generation by breaking waves—a laboratory study," in *Sea Surface Sound: Natural Mechanisms of Surface Generated Noise in the Ocean*, pp. 429–436, Springer, 1988.

[27] J. A. Nystuen, C. C. McGlothin, and M. S. Cook, "The underwater sound generated by heavy rainfall," *The Journal of the Acoustical Society of America*, vol. 93, no. 6, pp. 3169–3177, 1993.

[28] U. Zölzer, *Digital audio signal processing*. John Wiley & Sons, 2022.

[29] M. G. Christensen, *Introduction to audio processing*. Springer, 2019.

[30] S. F. Hussin, G. Birasamy, and Z. Hamid, "Design of butterworth band-pass filter," *Politeknik & Kolej Komuniti Journal of Engineering and Technology*, vol. 1, no. 1, pp. 32–46, 2016.

[31] P. V. Yadav, A. Alimohammad, and F. Harris, "Efficient design and implementation of energy detection-based spectrum sensing," *Circuits, Systems, and Signal Processing*, vol. 38, pp. 5187–5211, 2019.

[32] K. M. Prabhu, *Window functions and their applications in signal processing*. Taylor & Francis, 2014.

[33] U. Karrenberg, *Signale—Prozesse—Systeme: Eine multimediale und interaktive Einführung in die Signalverarbeitung*. Springer, 2012.

[34] M. Meyer, "Digitale signale," in *Signalverarbeitung: Analoge und digitale Signale, Systeme und Filter*, pp. 150–224, Springer, 2021.

[35] W. Wang, J. Wang, and C. Li, "A signal detection method based on hybrid energy detection," in *2022 4th International Conference on Intelligent Control, Measurement and Signal Processing (ICMSP)*, pp. 695–700, IEEE, 2022.

[36] A. Trnkoczy, "Understanding and parameter setting of sta/lta trigger algorithm," in *New manual of seismological observatory practice (NMSOP)*, pp. 1–20, Deutsches GeoForschungsZentrum GFZ, 2009.

[37] L. Gonçalves, A. Subtil, M. R. Oliveira, and P. de Zea Bermudez, "Roc curve estimation: An overview," *REVSTAT-Statistical journal*, vol. 12, no. 1, pp. 1–20, 2014.

[38] Z. H. Hoo, J. Candlish, and D. Teare, "What is an roc curve?," 2017.

[39] J. A. Hanley, "Receiver operating characteristic (roc) curves," *Wiley StatsRef: Statistics Reference Online*, 2014.

[40] S. Narkhede, "Understanding auc-roc curve," *Towards data science*, vol. 26, no. 1, pp. 220–227, 2018.

[41] S.-T. Yeh *et al.*, "Using trapezoidal rule for the area under a curve calculation," *Proceedings of the 27th Annual SAS® User Group International (SUGI'02)*, pp. 1–5, 2002.

A

Appendix 1

Table A.1: Complete set of all AUC values for the different combinations of STA, LTA, and Bandpass.

Lower Limit (Hz)	Upper Limit (Hz)	STA (min)	LTA (min)	AUC
30	250	4	10	0.709
250	1000	4	10	0.725
1000	4000	4	10	0.733
4000	20000	4	10	0.702
30	250	4	20	0.747
250	1000	4	20	0.765
1000	4000	4	20	0.759
4000	20000	4	20	0.737
30	250	4	30	0.775
250	1000	4	30	0.795
1000	4000	4	30	0.786
4000	20000	4	30	0.749
30	250	4	40	0.771
250	1000	4	40	0.801
1000	4000	4	40	0.794
4000	20000	4	40	0.758
30	250	4	50	0.765
250	1000	4	50	0.813
1000	4000	4	50	0.807
4000	20000	4	50	0.772
30	250	4	60	0.758
250	1000	4	60	0.813
1000	4000	4	60	0.798
4000	20000	4	60	0.765
30	250	4	70	0.762
250	1000	4	70	0.819
1000	4000	4	70	0.809
4000	20000	4	70	0.77
30	250	4	80	0.756
250	1000	4	80	0.825
1000	4000	4	80	0.815

Lower Limit (Hz)	Upper Limit (Hz)	STA (min)	LTA (min)	AUC
4000	20000	4	80	0.774
30	250	4	90	0.758
250	1000	4	90	0.83
1000	4000	4	90	0.82
4000	20000	4	90	0.78
30	250	4	100	0.755
250	1000	4	100	0.83
1000	4000	4	100	0.82
4000	20000	4	100	0.78
30	250	4	110	0.756
250	1000	4	110	0.831
1000	4000	4	110	0.82
4000	20000	4	110	0.778
30	250	4	120	0.755
250	1000	4	120	0.826
1000	4000	4	120	0.814
4000	20000	4	120	0.775
30	250	4	130	0.759
250	1000	4	130	0.827
1000	4000	4	130	0.82
4000	20000	4	130	0.779
30	250	4	140	0.776
250	1000	4	140	0.827
1000	4000	4	140	0.825
4000	20000	4	140	0.778
30	250	4	150	0.775
250	1000	4	150	0.831
1000	4000	4	150	0.837
4000	20000	4	150	0.783
30	250	4	160	0.775
250	1000	4	160	0.827
1000	4000	4	160	0.831
4000	20000	4	160	0.78
30	250	4	170	0.782
250	1000	4	170	0.832
1000	4000	4	170	0.837
4000	20000	4	170	0.784
30	250	4	180	0.779
250	1000	4	180	0.831
1000	4000	4	180	0.838
4000	20000	4	180	0.786
30	250	4	190	0.77
250	1000	4	190	0.831
1000	4000	4	190	0.836

Lower Limit (Hz)	Upper Limit (Hz)	STA (min)	LTA (min)	AUC
4000	20000	4	190	0.784
30	250	4	200	0.763
250	1000	4	200	0.828
1000	4000	4	200	0.834
4000	20000	4	200	0.784
30	250	3	10	0.705
250	1000	3	10	0.724
1000	4000	3	10	0.723
4000	20000	3	10	0.684
30	250	3	20	0.797
250	1000	3	20	0.843
1000	4000	3	20	0.838
4000	20000	3	20	0.789
30	250	3	30	0.828
250	1000	3	30	0.871
1000	4000	3	30	0.862
4000	20000	3	30	0.804
30	250	3	40	0.831
250	1000	3	40	0.879
1000	4000	3	40	0.868
4000	20000	3	40	0.804
30	250	3	50	0.834
250	1000	3	50	0.885
1000	4000	3	50	0.884
4000	20000	3	50	0.822
30	250	3	60	0.848
250	1000	3	60	0.892
1000	4000	3	60	0.89
4000	20000	3	60	0.829
30	250	3	70	0.851
250	1000	3	70	0.89
1000	4000	3	70	0.891
4000	20000	3	70	0.833
30	250	3	80	0.847
250	1000	3	80	0.891
1000	4000	3	80	0.892
4000	20000	3	80	0.837
30	250	3	90	0.838
250	1000	3	90	0.897
1000	4000	3	90	0.893
4000	20000	3	90	0.84
30	250	3	100	0.836
250	1000	3	100	0.898
1000	4000	3	100	0.894

Lower Limit (Hz)	Upper Limit (Hz)	STA (min)	LTA (min)	AUC
4000	20000	3	100	0.84
30	250	3	110	0.836
250	1000	3	110	0.902
1000	4000	3	110	0.899
4000	20000	3	110	0.841
30	250	3	120	0.841
250	1000	3	120	0.902
1000	4000	3	120	0.902
4000	20000	3	120	0.841
30	250	3	130	0.844
250	1000	3	130	0.903
1000	4000	3	130	0.905
4000	20000	3	130	0.843
30	250	3	140	0.851
250	1000	3	140	0.906
1000	4000	3	140	0.908
4000	20000	3	140	0.843
30	250	3	150	0.857
250	1000	3	150	0.908
1000	4000	3	150	0.91
4000	20000	3	150	0.843
30	250	3	160	0.858
250	1000	3	160	0.907
1000	4000	3	160	0.912
4000	20000	3	160	0.843
30	250	3	170	0.857
250	1000	3	170	0.908
1000	4000	3	170	0.912
4000	20000	3	170	0.843
30	250	3	180	0.857
250	1000	3	180	0.907
1000	4000	3	180	0.91
4000	20000	3	180	0.844
30	250	3	190	0.856
250	1000	3	190	0.906
1000	4000	3	190	0.911
4000	20000	3	190	0.844
30	250	3	200	0.854
250	1000	3	200	0.903
1000	4000	3	200	0.909
4000	20000	3	200	0.843
30	250	2	10	0.741
250	1000	2	10	0.766
1000	4000	2	10	0.747

Lower Limit (Hz)	Upper Limit (Hz)	STA (min)	LTA (min)	AUC
4000	20000	2	10	0.699
30	250	2	20	0.81
250	1000	2	20	0.836
1000	4000	2	20	0.82
4000	20000	2	20	0.785
30	250	2	30	0.862
250	1000	2	30	0.857
1000	4000	2	30	0.835
4000	20000	2	30	0.802
30	250	2	40	0.835
250	1000	2	40	0.865
1000	4000	2	40	0.844
4000	20000	2	40	0.804
30	250	2	50	0.837
250	1000	2	50	0.877
1000	4000	2	50	0.854
4000	20000	2	50	0.814
30	250	2	60	0.838
250	1000	2	60	0.884
1000	4000	2	60	0.859
4000	20000	2	60	0.816
30	250	2	70	0.841
250	1000	2	70	0.889
1000	4000	2	70	0.862
4000	20000	2	70	0.816
30	250	2	80	0.845
250	1000	2	80	0.897
1000	4000	2	80	0.869
4000	20000	2	80	0.82
30	250	2	90	0.843
250	1000	2	90	0.896
1000	4000	2	90	0.86
4000	20000	2	90	0.818
30	250	2	100	0.844
250	1000	2	100	0.893
1000	4000	2	100	0.85
4000	20000	2	100	0.814
30	250	2	110	0.849
250	1000	2	110	0.895
1000	4000	2	110	0.852
4000	20000	2	110	0.814
30	250	2	120	0.854
250	1000	2	120	0.898
1000	4000	2	120	0.857

Lower Limit (Hz)	Upper Limit (Hz)	STA (min)	LTA (min)	AUC
4000	20000	2	120	0.815
30	250	2	130	0.832
250	1000	2	130	0.884
1000	4000	2	130	0.843
4000	20000	2	130	0.802
30	250	2	140	0.856
250	1000	2	140	0.899
1000	4000	2	140	0.862
4000	20000	2	140	0.818
30	250	2	150	0.858
250	1000	2	150	0.899
1000	4000	2	150	0.863
4000	20000	2	150	0.818
30	250	2	160	0.859
250	1000	2	160	0.899
1000	4000	2	160	0.862
4000	20000	2	160	0.818
30	250	2	170	0.859
250	1000	2	170	0.901
1000	4000	2	170	0.861
4000	20000	2	170	0.818
30	250	2	180	0.855
250	1000	2	180	0.901
1000	4000	2	180	0.86
4000	20000	2	180	0.819
30	250	2	190	0.853
250	1000	2	190	0.901
1000	4000	2	190	0.856
4000	20000	2	190	0.818
30	250	2	200	0.852
250	1000	2	200	0.9
1000	4000	2	200	0.856
4000	20000	2	200	0.817
30	250	1	10	0.713
250	1000	1	10	0.753
1000	4000	1	10	0.745
4000	20000	1	10	0.734
30	250	1	20	0.783
250	1000	1	20	0.834
1000	4000	1	20	0.826
4000	20000	1	20	0.81
30	250	1	30	0.81
250	1000	1	30	0.856
1000	4000	1	30	0.839

Lower Limit (Hz)	Upper Limit (Hz)	STA (min)	LTA (min)	AUC
4000	20000	1	30	0.814
30	250	1	40	0.816
250	1000	1	40	0.85
1000	4000	1	40	0.837
4000	20000	1	40	0.808
30	250	1	50	0.819
250	1000	1	50	0.855
1000	4000	1	50	0.844
4000	20000	1	50	0.811
30	250	1	60	0.824
250	1000	1	60	0.859
1000	4000	1	60	0.851
4000	20000	1	60	0.816
30	250	1	70	0.828
250	1000	1	70	0.864
1000	4000	1	70	0.855
4000	20000	1	70	0.819
30	250	1	80	0.828
250	1000	1	80	0.87
1000	4000	1	80	0.858
4000	20000	1	80	0.82
30	250	1	90	0.825
250	1000	1	90	0.87
1000	4000	1	90	0.851
4000	20000	1	90	0.821
30	250	1	100	0.822
250	1000	1	100	0.868
1000	4000	1	100	0.84
4000	20000	1	100	0.815
30	250	1	110	0.825
250	1000	1	110	0.872
1000	4000	1	110	0.843
4000	20000	1	110	0.814
30	250	1	120	0.831
250	1000	1	120	0.877
1000	4000	1	120	0.846
4000	20000	1	120	0.813
30	250	1	130	0.835
250	1000	1	130	0.879
1000	4000	1	130	0.852
4000	20000	1	130	0.814
30	250	1	140	0.839
250	1000	1	140	0.879
1000	4000	1	140	0.854

Lower Limit (Hz)	**Upper Limit (Hz)**	**STA (min)**	**LTA (min)**	**AUC**
4000	20000	1	140	0.815
30	250	1	150	0.842
250	1000	1	150	0.878
1000	4000	1	150	0.856
4000	20000	1	150	0.814
30	250	1	160	0.846
250	1000	1	160	0.879
1000	4000	1	160	0.859
4000	20000	1	160	0.816
30	250	1	170	0.847
250	1000	1	170	0.88
1000	4000	1	170	0.86
4000	20000	1	170	0.815
30	250	1	180	0.847
250	1000	1	180	0.88
1000	4000	1	180	0.86
4000	20000	1	180	0.815
30	250	1	190	0.844
250	1000	1	190	0.88
1000	4000	1	190	0.858
4000	20000	1	190	0.814
30	250	1	200	0.841
250	1000	1	200	0.877
1000	4000	1	200	0.858
4000	20000	1	200	0.814

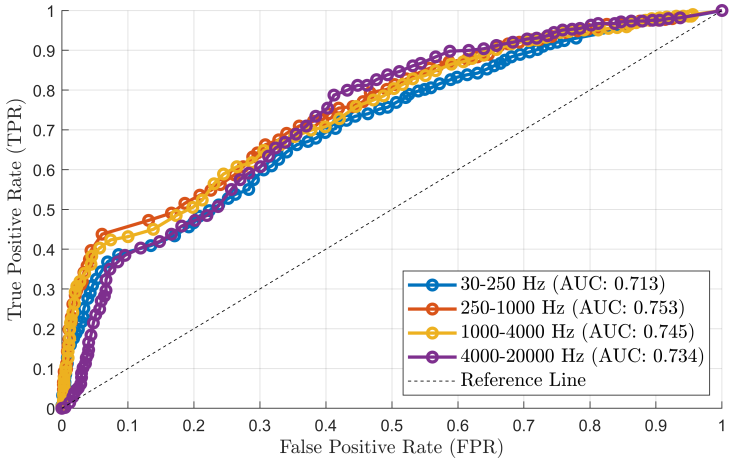

Figure A.1: The ROC curve for an STA of 1 minute and an LTA of 10 minutes

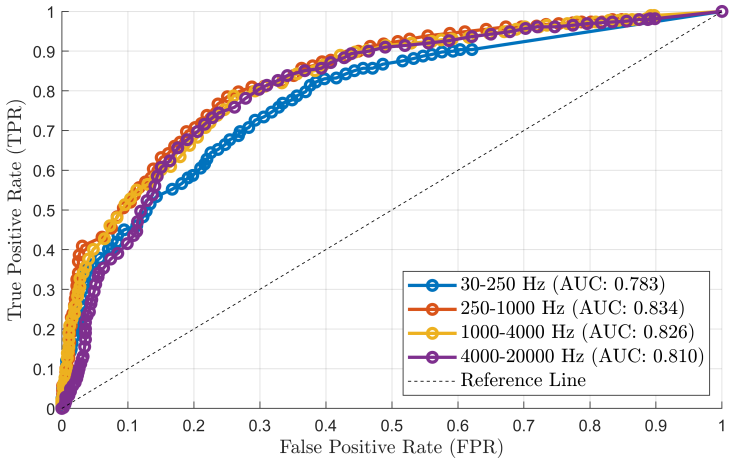

Figure A.2: The ROC curve for an STA of 1 minute and an LTA of 20 minutes

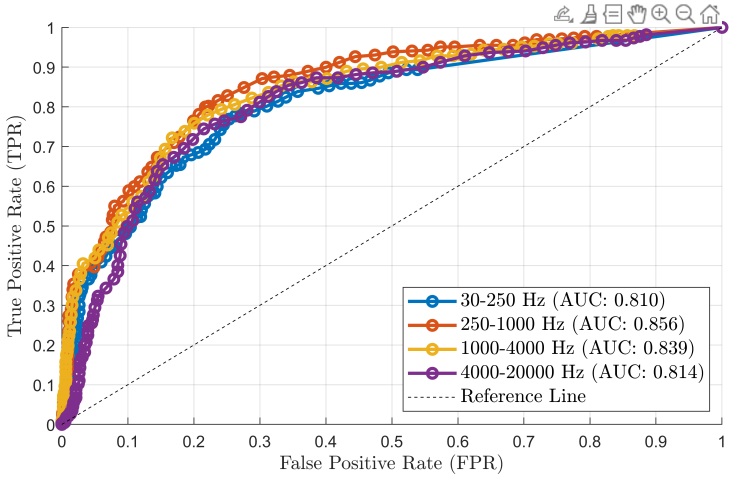

Figure A.3: The ROC curve for an STA of 1 minute and an LTA of 30 minutes

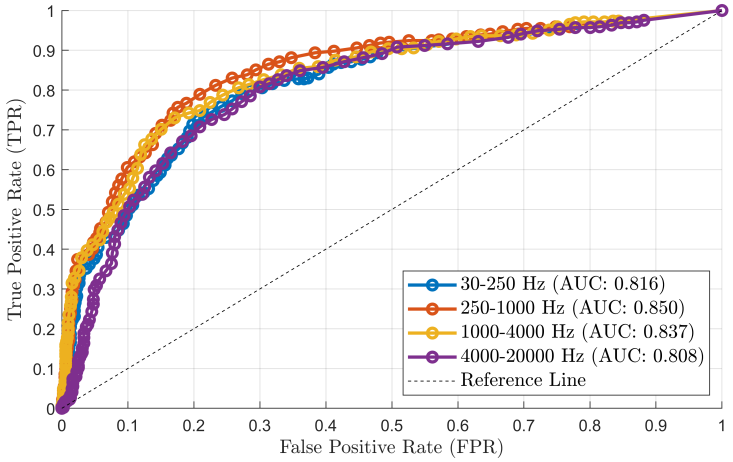

Figure A.4: The ROC curve for an STA of 1 minute and an LTA of 40 minutes

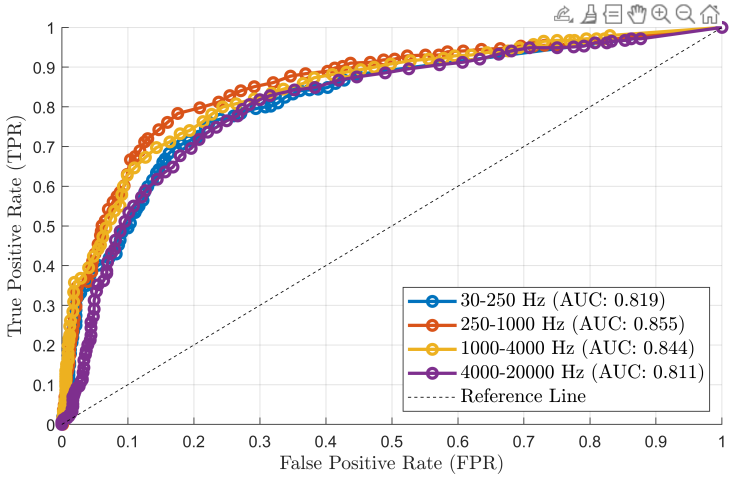

Figure A.5: The ROC curve for an STA of 1 minute and an LTA of 50 minutes

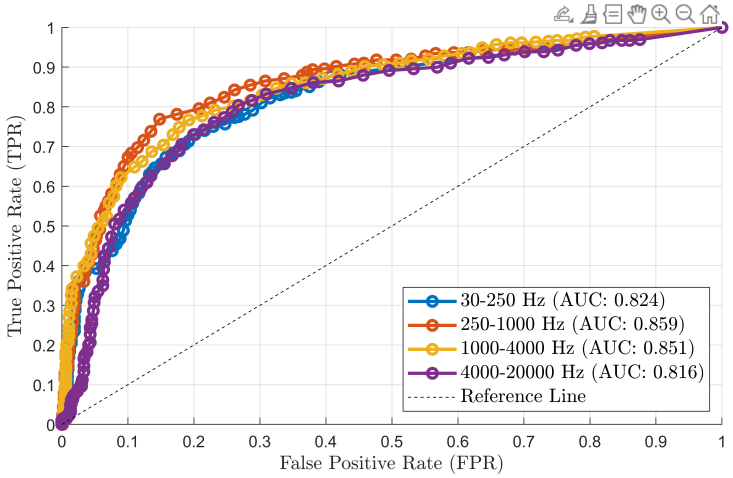

Figure A.6: The ROC curve for an STA of 1 minute and an LTA of 60 minutes

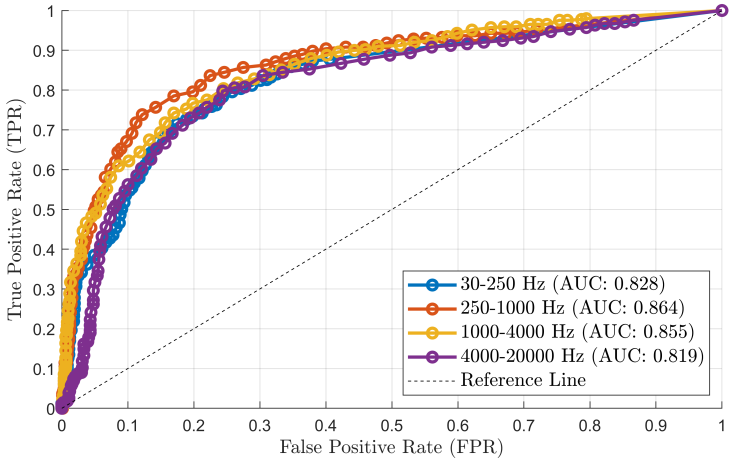

Figure A.7: The ROC curve for an STA of 1 minute and an LTA of 70 minutes

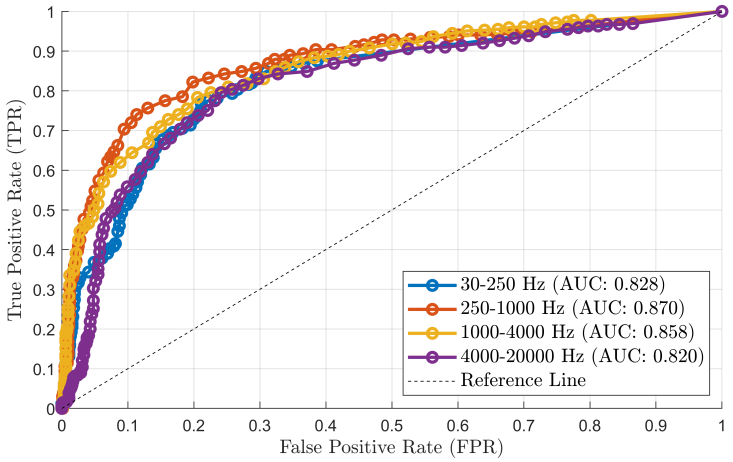

Figure A.8: The ROC curve for an STA of 1 minute and an LTA of 80 minutes

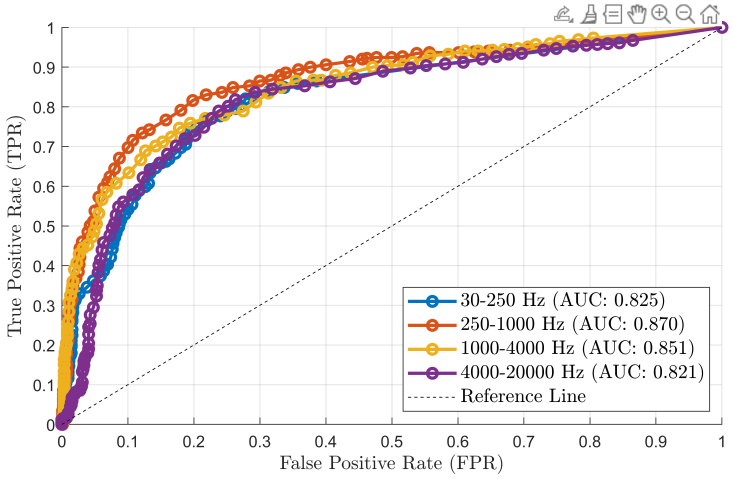

Figure A.9: The ROC curve for an STA of 1 minute and an LTA of 90 minutes

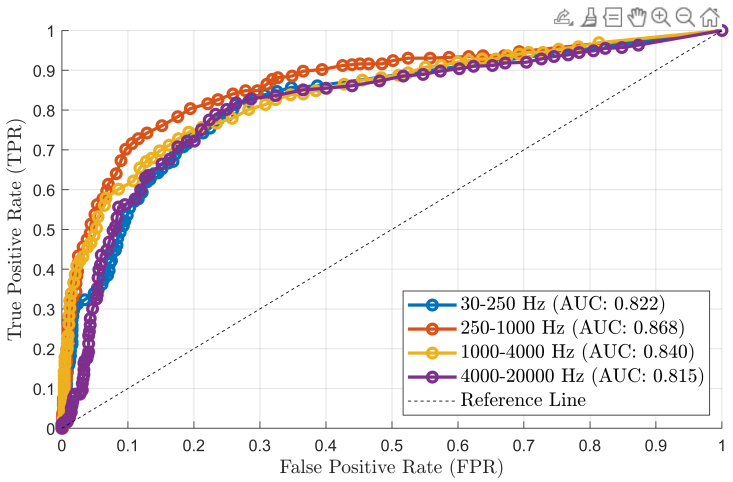

Figure A.10: The ROC curve for an STA of 1 minute and an LTA of 100 minutes

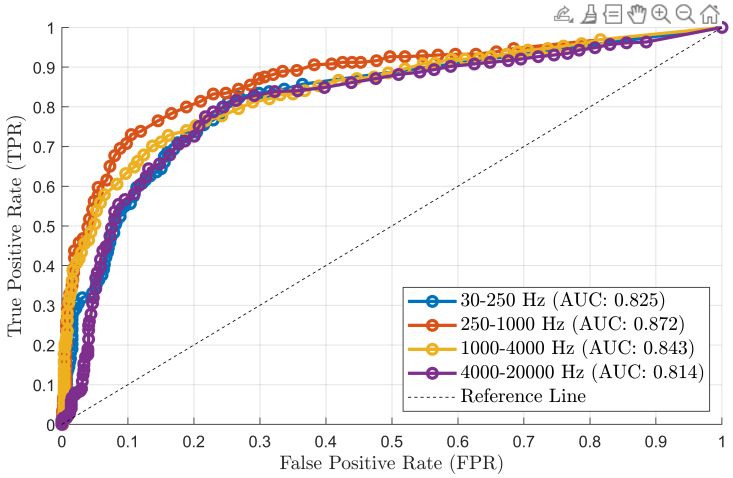

Figure A.11: The ROC curve for an STA of 1 minute and an LTA of 110 minutes

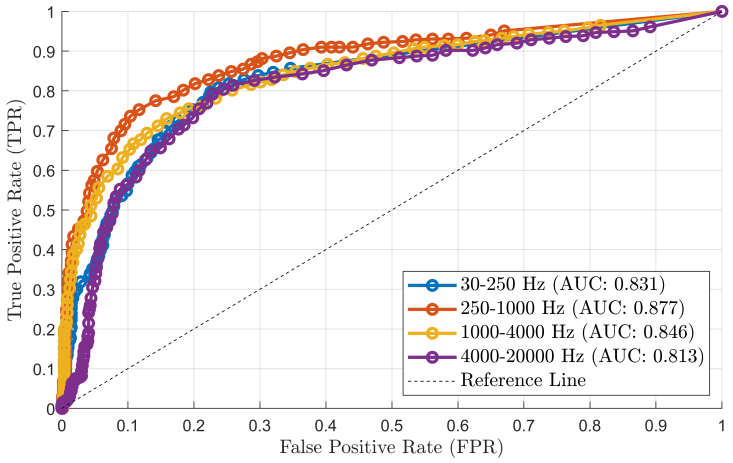

Figure A.12: The ROC curve for an STA of 1 minute and an LTA of 120 minutes

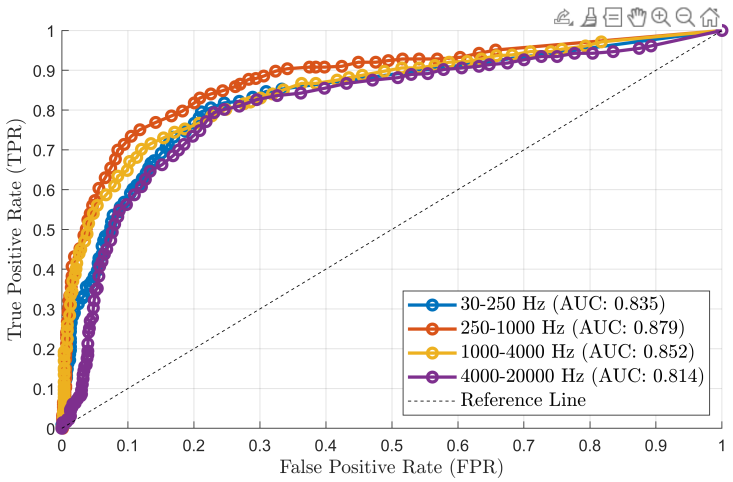

Figure A.13: The ROC curve for an STA of 1 minute and an LTA of 130 minutes

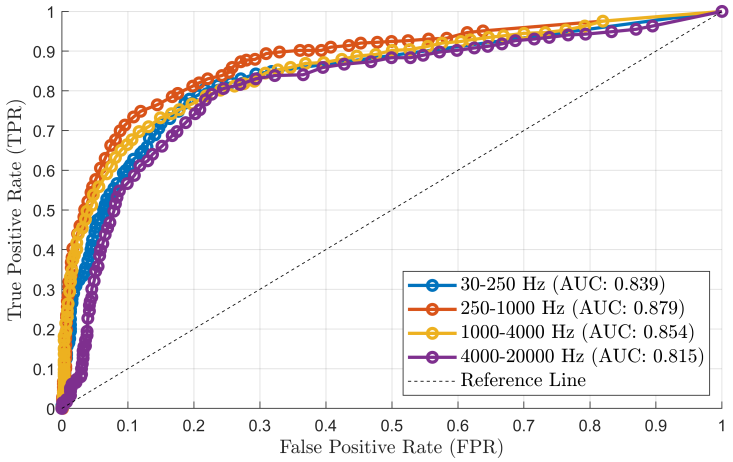

Figure A.14: The ROC curve for an STA of 1 minute and an LTA of 140 minutes

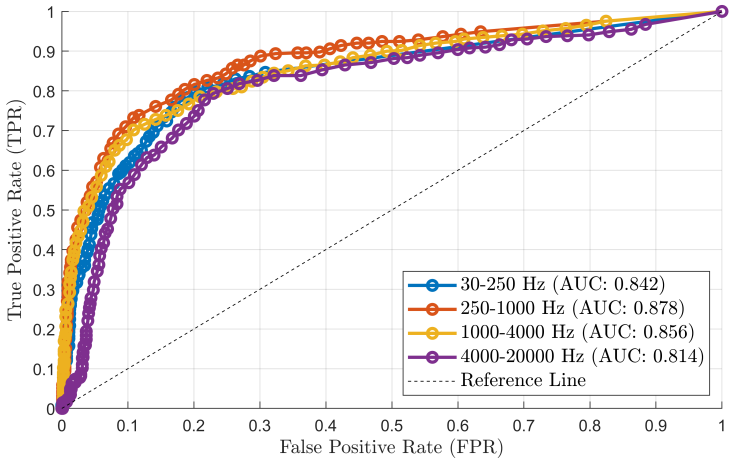

Figure A.15: The ROC curve for an STA of 1 minute and an LTA of 150 minutes

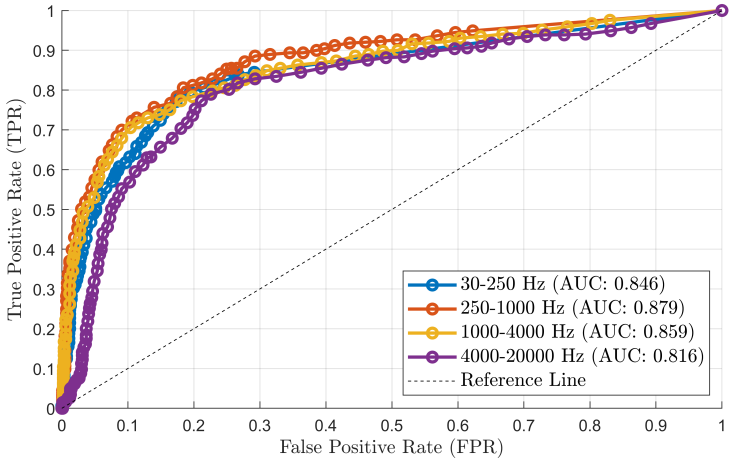

Figure A.16: The ROC curve for an STA of 1 minute and an LTA of 160 minutes

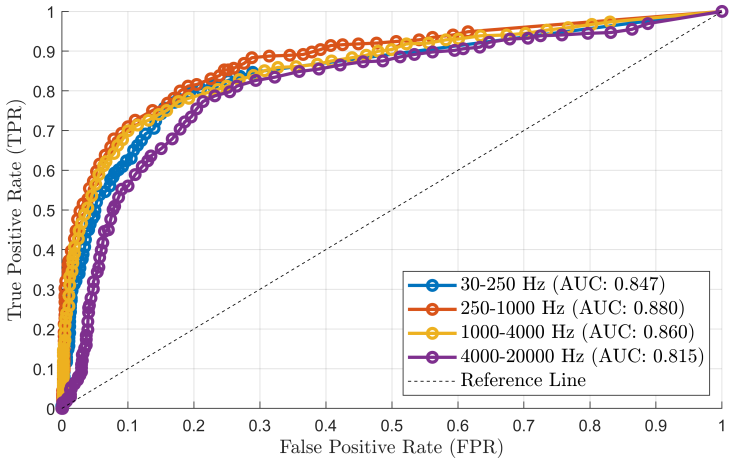

Figure A.17: The ROC curve for an STA of 1 minute and an LTA of 170 minutes

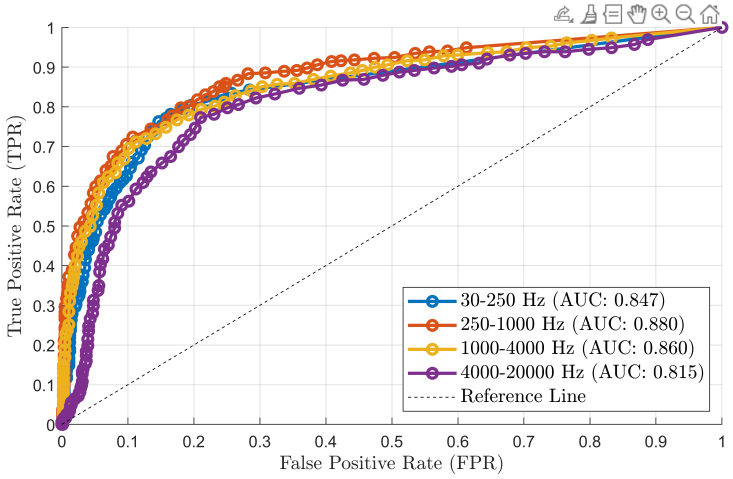

Figure A.18: The ROC curve for an STA of 1 minute and an LTA of 180 minutes

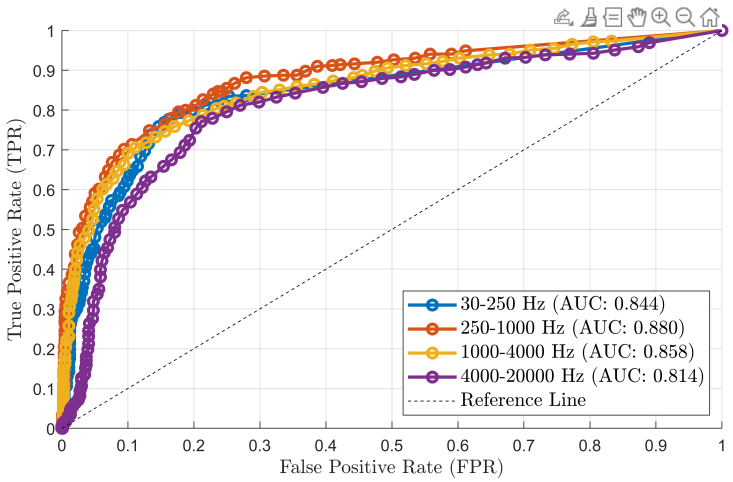

Figure A.19: The ROC curve for an STA of 1 minute and an LTA of 190 minutes

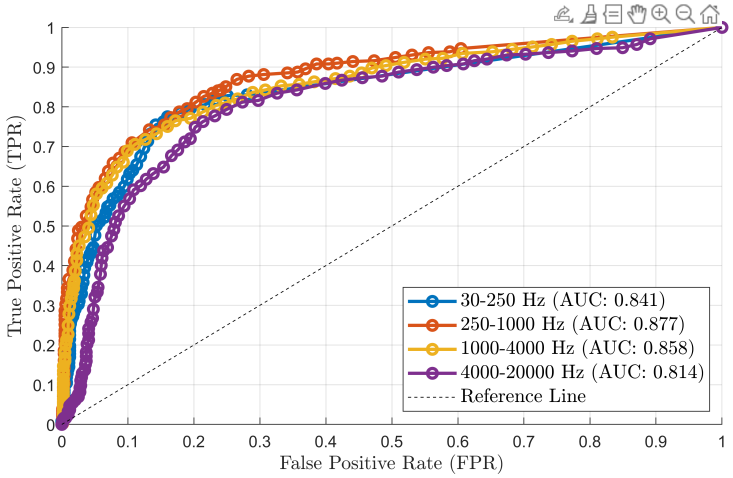

Figure A.20: The ROC curve for an STA of 1 minute and an LTA of 200 minutes

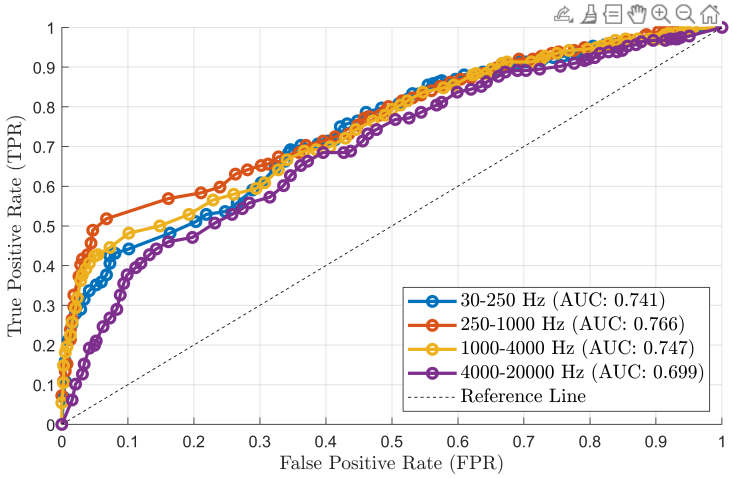

Figure A.21: The ROC curve for an STA of 2 minute and an LTA of 10 minutes

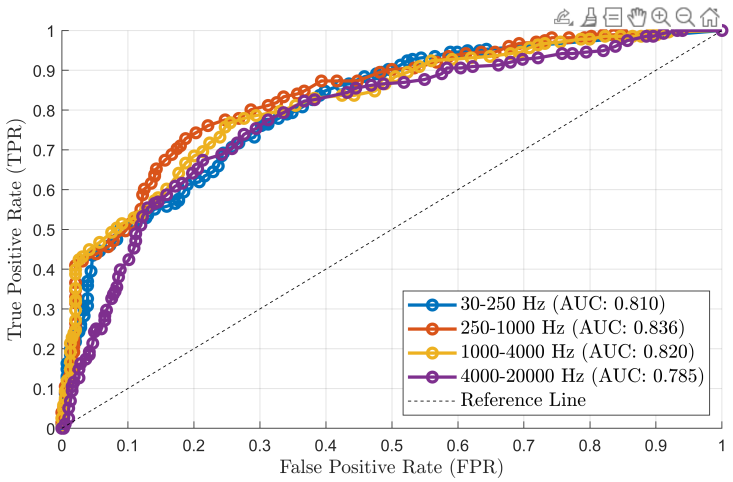

Figure A.22: The ROC curve for an STA of 2 minute and an LTA of 20 minutes

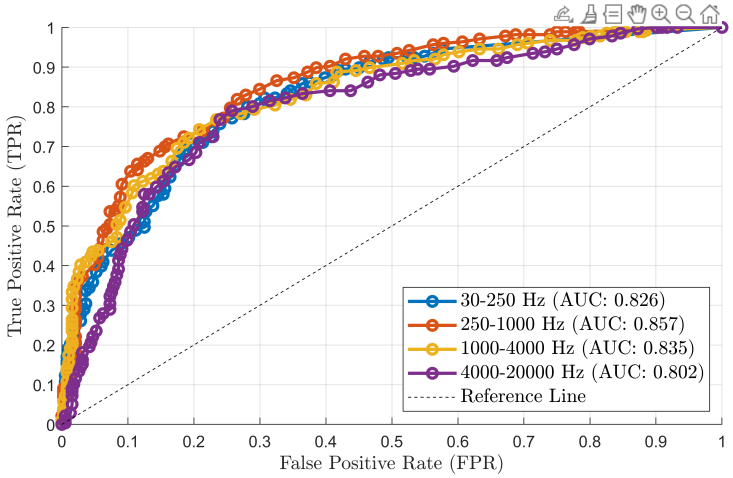

Figure A.23: The ROC curve for an STA of 2 minute and an LTA of 30 minutes

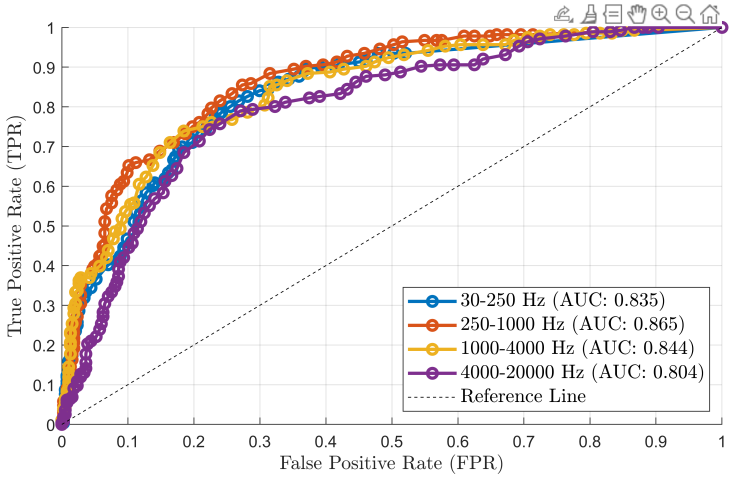

Figure A.24: The ROC curve for an STA of 2 minute and an LTA of 40 minutes

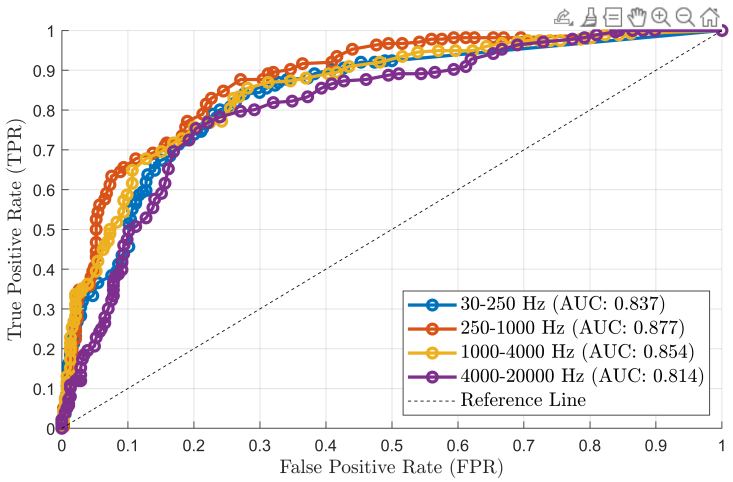

Figure A.25: The ROC curve for an STA of 2 minute and an LTA of 50 minutes

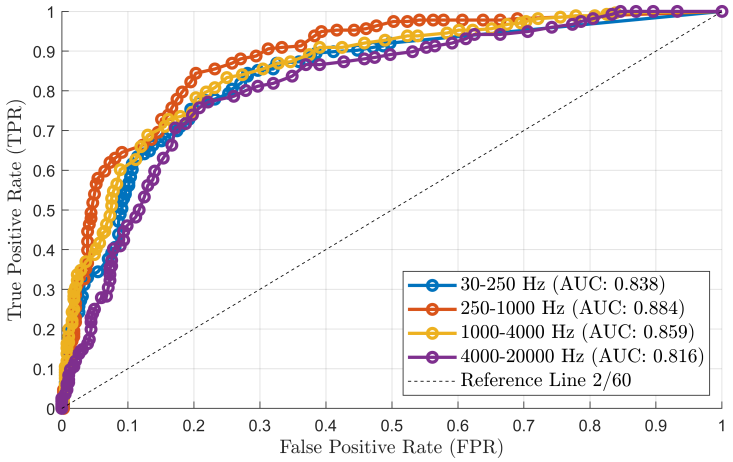

Figure A.26: The ROC curve for an STA of 2 minute and an LTA of 60 minutes

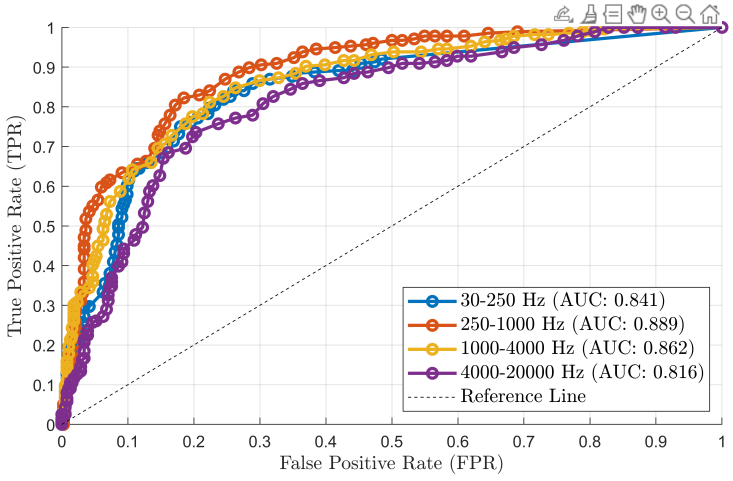

Figure A.27: The ROC curve for an STA of 2 minute and an LTA of 70 minutes

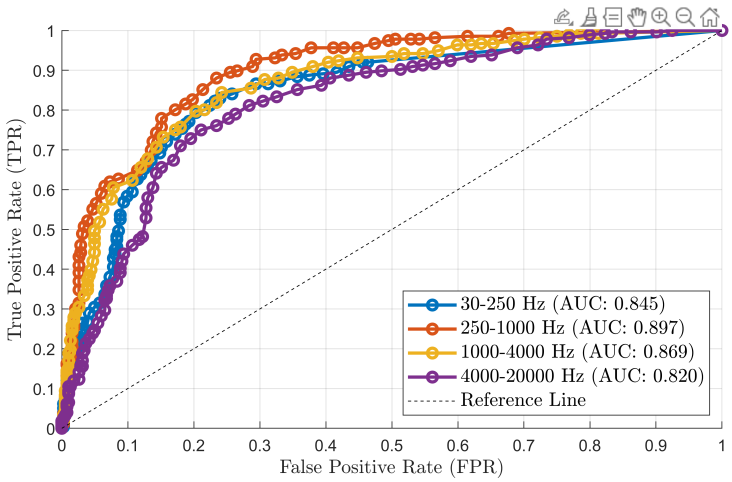

Figure A.28: The ROC curve for an STA of 2 minute and an LTA of 80 minutes

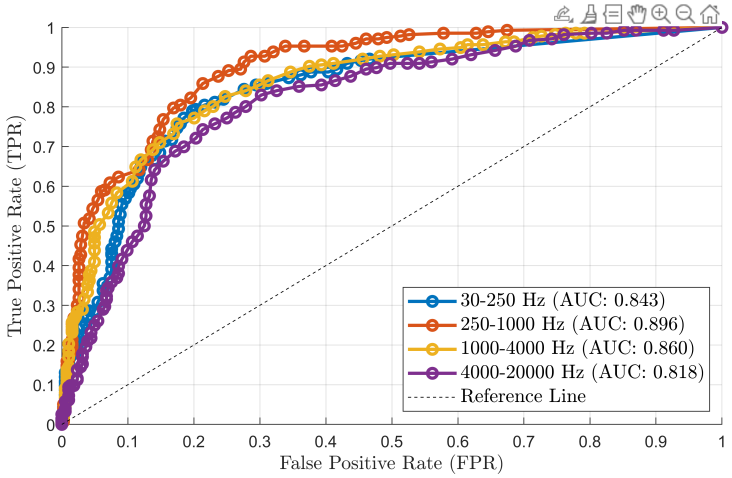

Figure A.29: The ROC curve for an STA of 2 minute and an LTA of 90 minutes

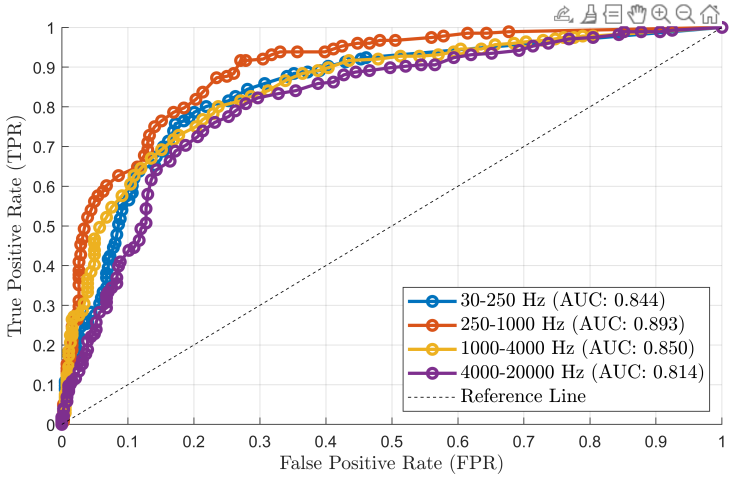

Figure A.30: The ROC curve for an STA of 2 minutes and an LTA of 100 minutes

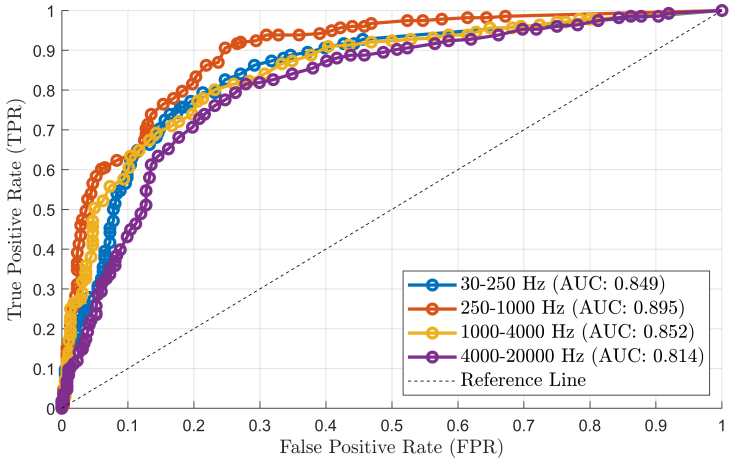

Figure A.31: The ROC curve for an STA of 2 minutes and an LTA of 110 minutes

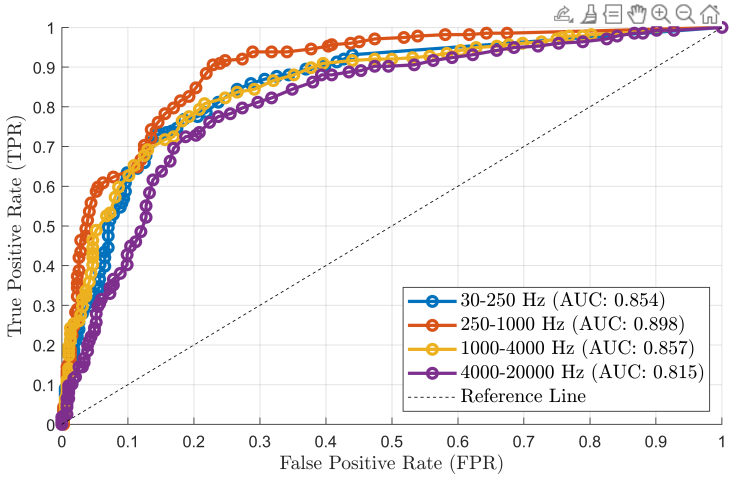

Figure A.32: The ROC curve for an STA of 2 minutes and an LTA of 120 minutes

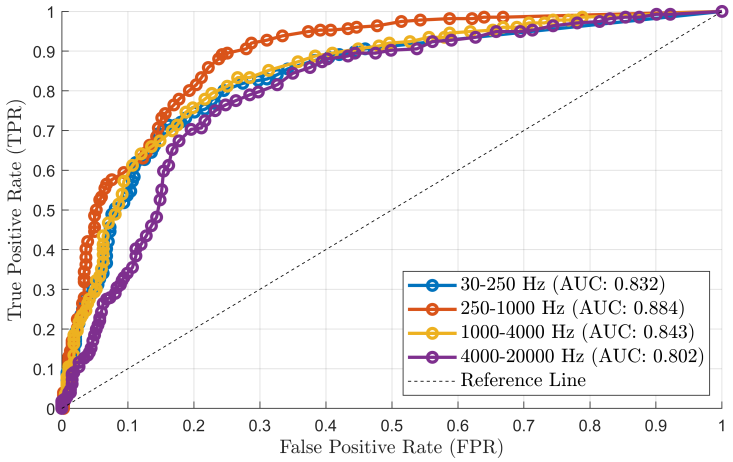

Figure A.33: The ROC curve for an STA of 2 minutes and an LTA of 130 minutes

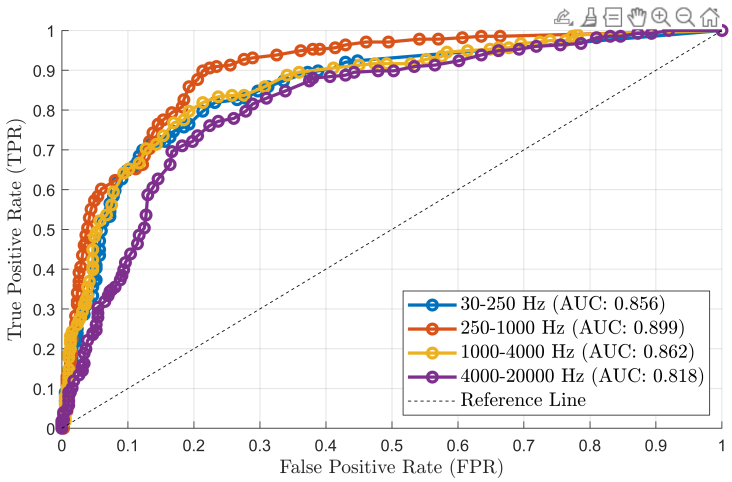

Figure A.34: The ROC curve for an STA of 2 minutes and an LTA of 140 minutes

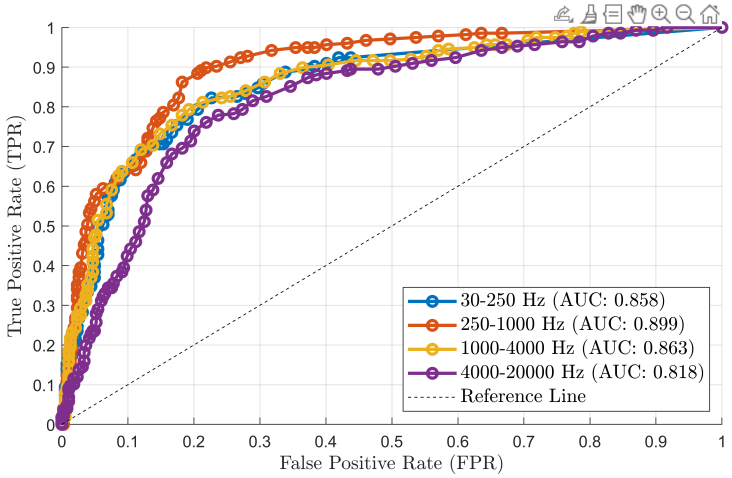

Figure A.35: The ROC curve for an STA of 2 minutes and an LTA of 150 minutes

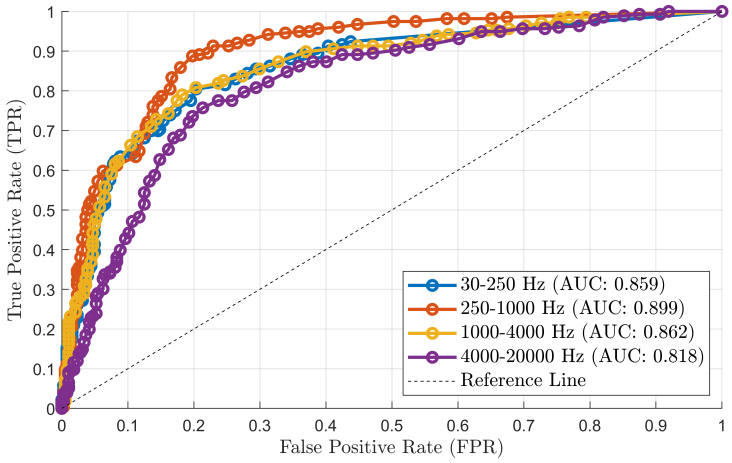

Figure A.36: The ROC curve for an STA of 2 minutes and an LTA of 160 minutes

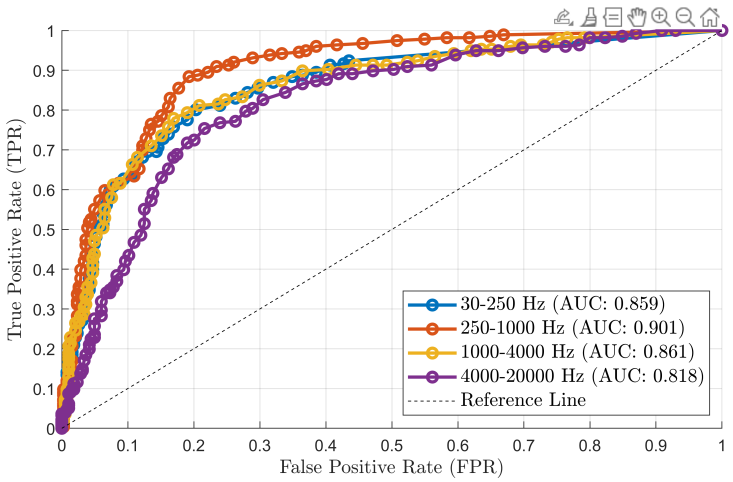

Figure A.37: The ROC curve for an STA of 2 minutes and an LTA of 170 minutes

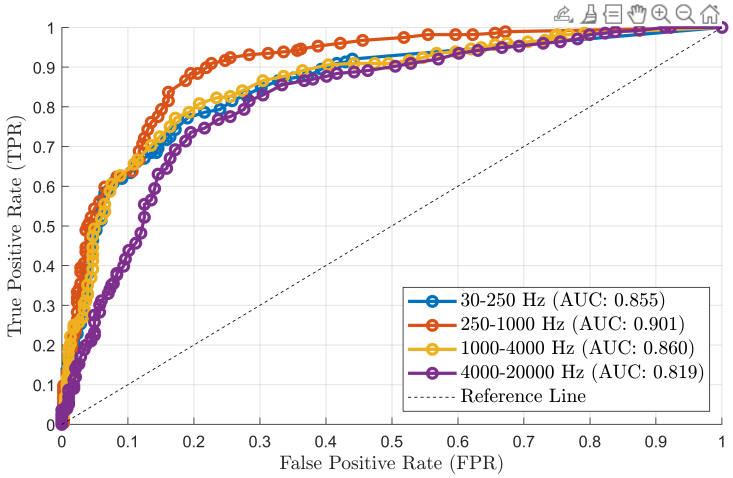

Figure A.38: The ROC curve for an STA of 2 minutes and an LTA of 180 minutes

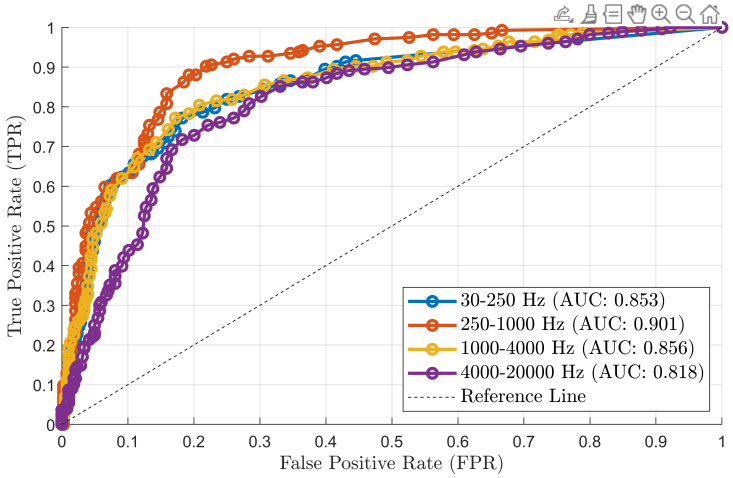

Figure A.39: The ROC curve for an STA of 2 minutes and an LTA of 190 minutes

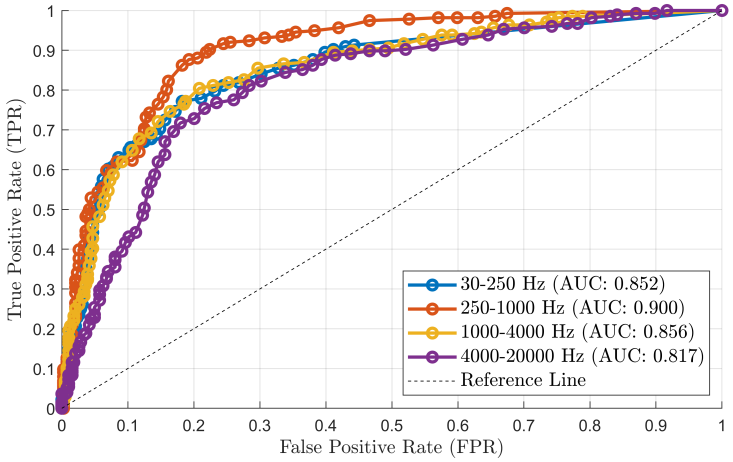

Figure A.40: The ROC curve for an STA of 2 minutes and an LTA of 200 minutes

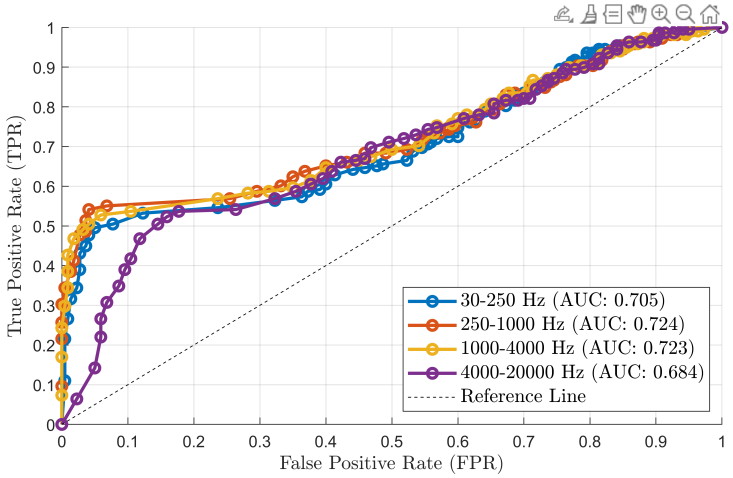

Figure A.41: The ROC curve for an STA of 3 minute and an LTA of 10 minutes

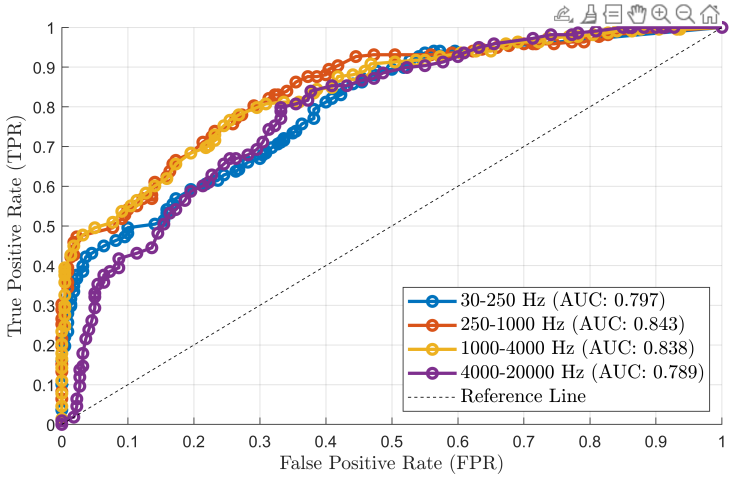

Figure A.42: The ROC curve for an STA of 3 minute and an LTA of 20 minutes

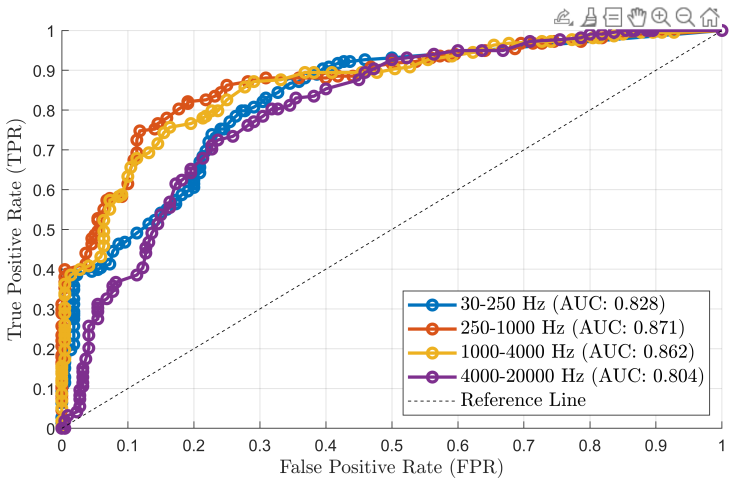

Figure A.43: The ROC curve for an STA of 3 minute and an LTA of 30 minutes

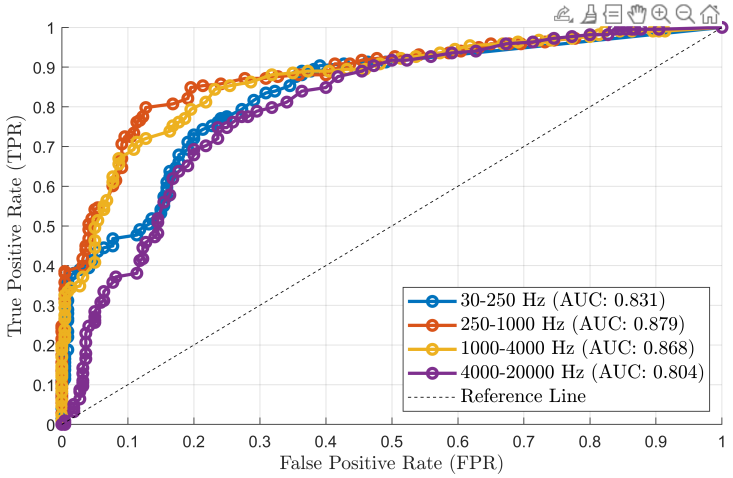

Figure A.44: The ROC curve for an STA of 3 minute and an LTA of 40 minutes

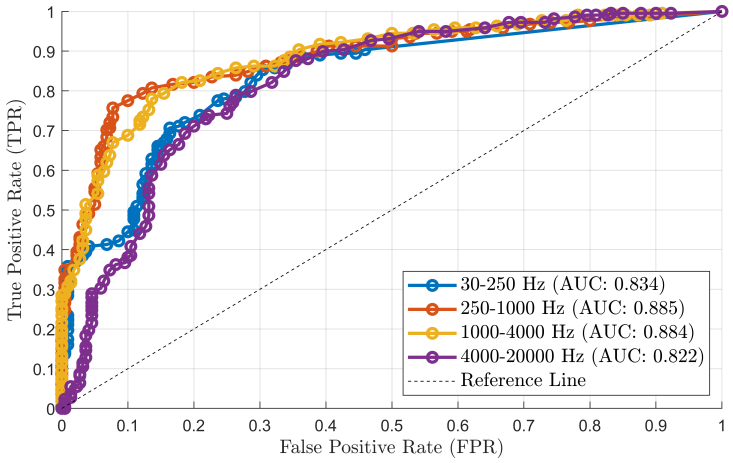

Figure A.45: The ROC curve for an STA of 3 minute and an LTA of 50 minutes

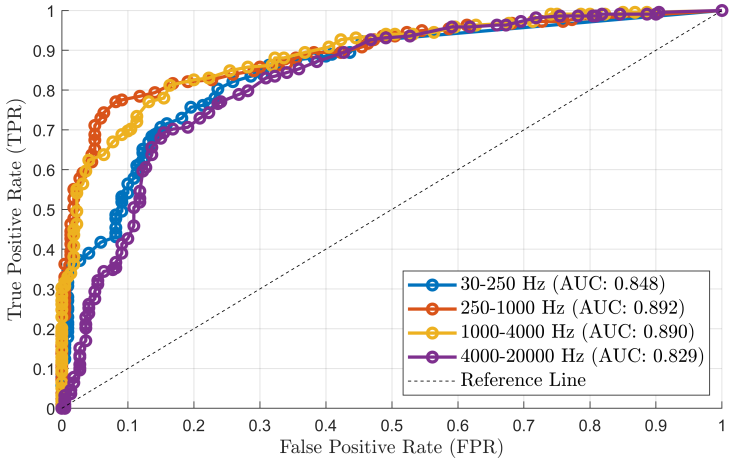

Figure A.46: The ROC curve for an STA of 3 minute and an LTA of 60 minutes

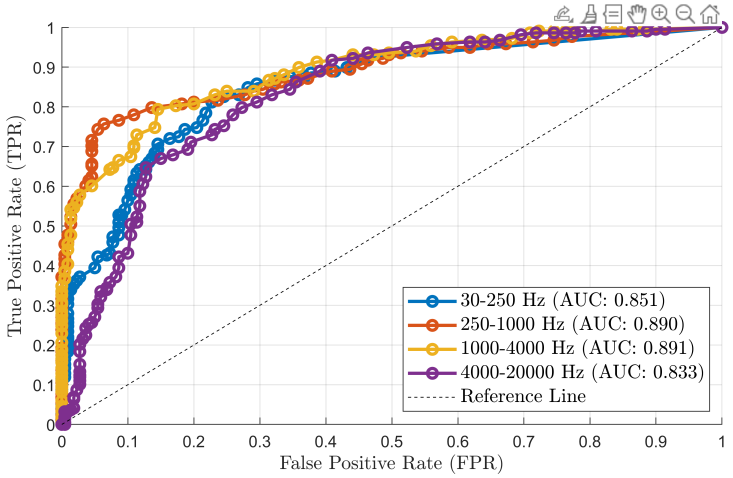

Figure A.47: The ROC curve for an STA of 3 minute and an LTA of 70 minutes

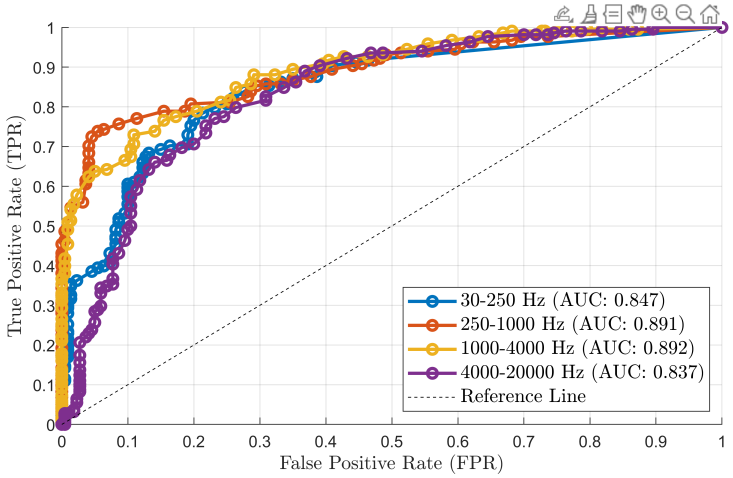

Figure A.48: The ROC curve for an STA of 3 minute and an LTA of 80 minutes

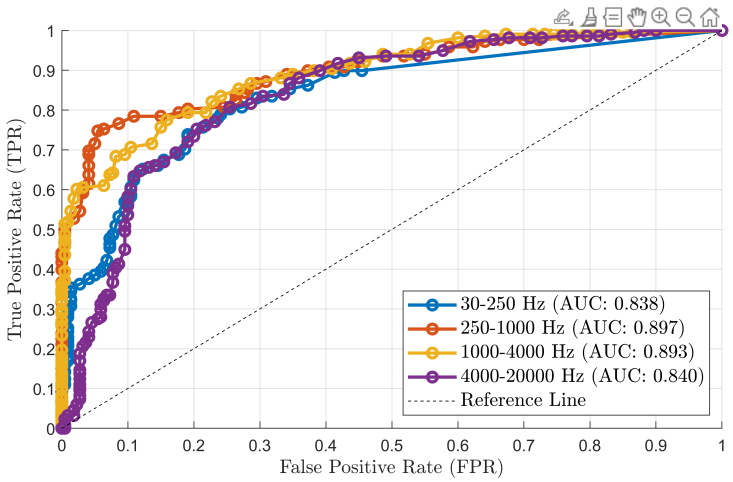

Figure A.49: The ROC curve for an STA of 3 minute and an LTA of 90 minutes

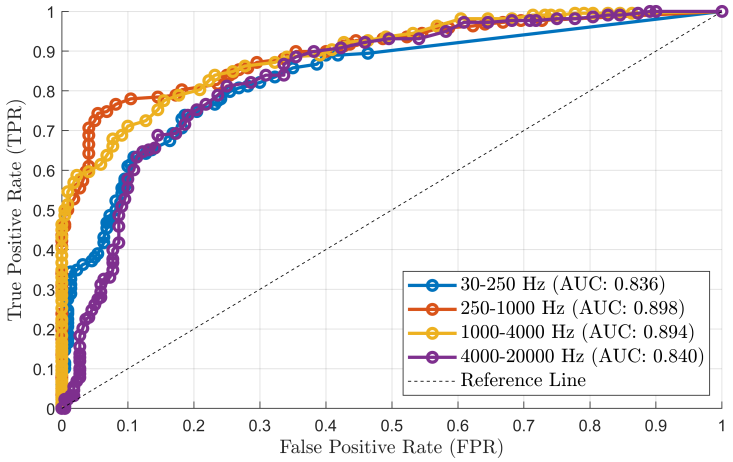

Figure A.50: The ROC curve for an STA of 3 minutes and an LTA of 100 minutes

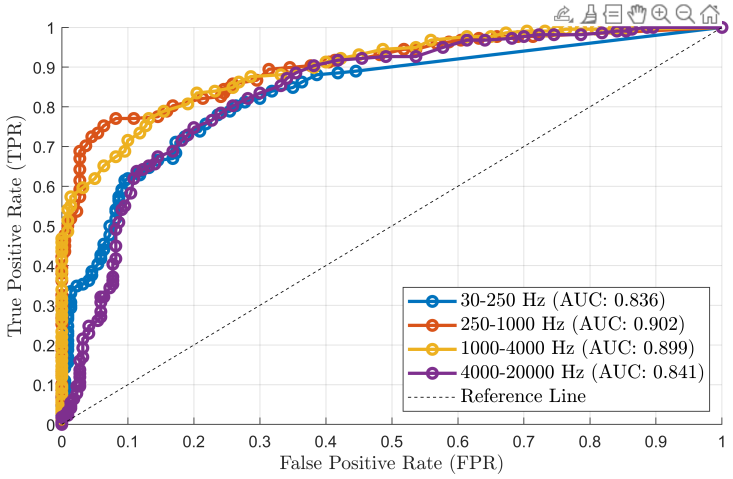

Figure A.51: The ROC curve for an STA of 3 minutes and an LTA of 110 minutes

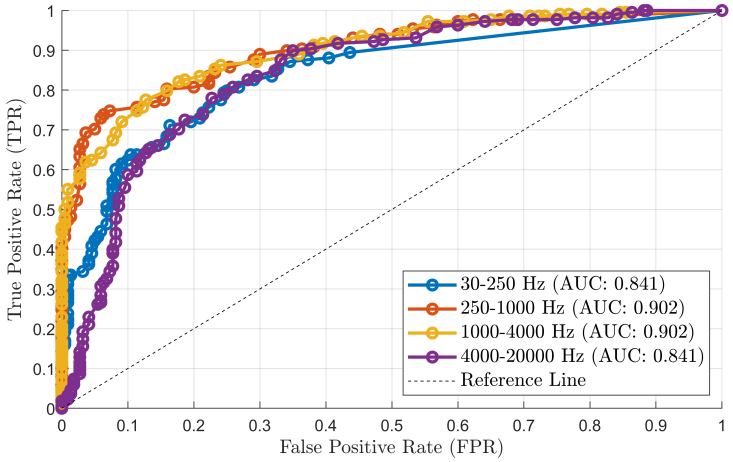

Figure A.52: The ROC curve for an STA of 3 minutes and an LTA of 120 minutes

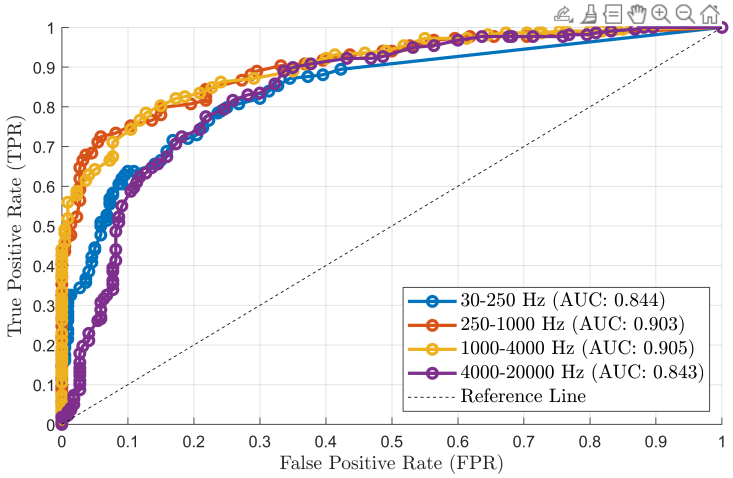

Figure A.53: The ROC curve for an STA of 3 minutes and an LTA of 130 minutes

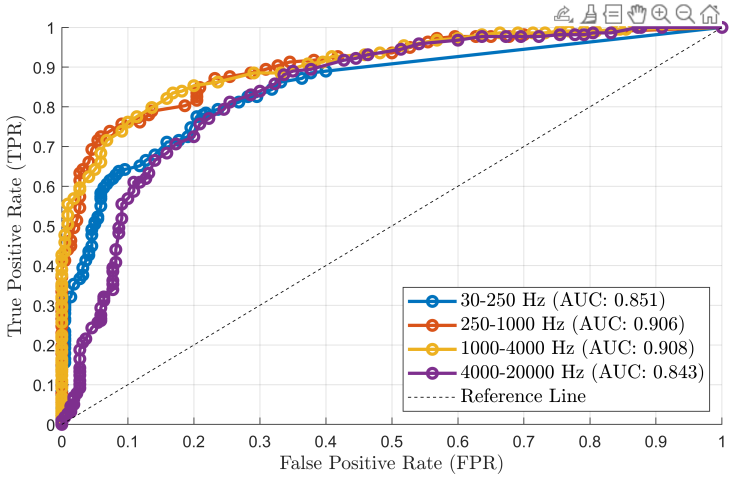

Figure A.54: The ROC curve for an STA of 3 minutes and an LTA of 140 minutes

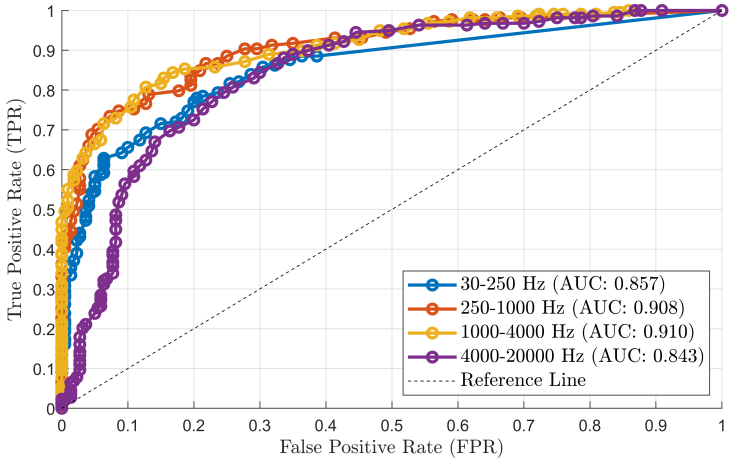

Figure A.55: The ROC curve for an STA of 3 minutes and an LTA of 150 minutes

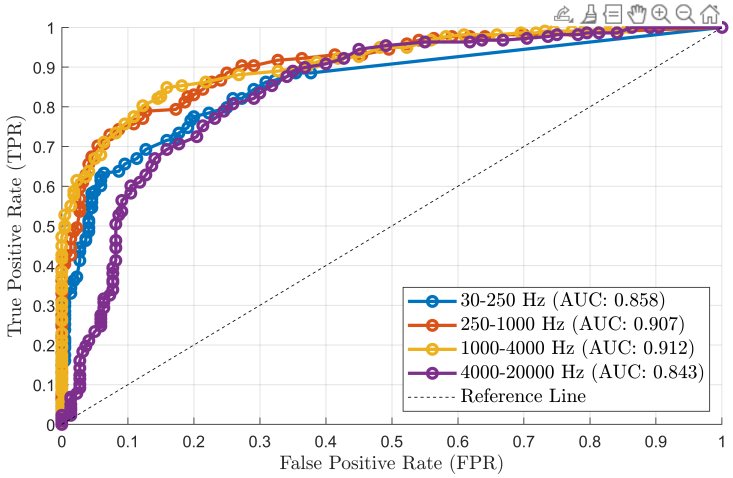

Figure A.56: The ROC curve for an STA of 3 minutes and an LTA of 160 minutes

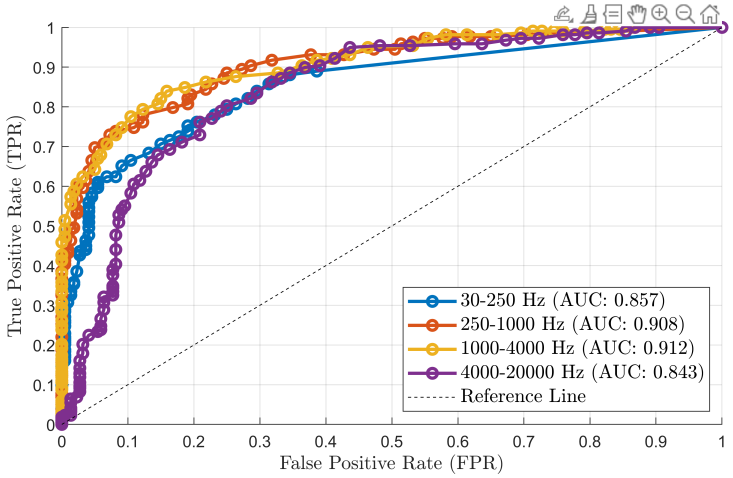

Figure A.57: The ROC curve for an STA of 3 minutes and an LTA of 170 minutes

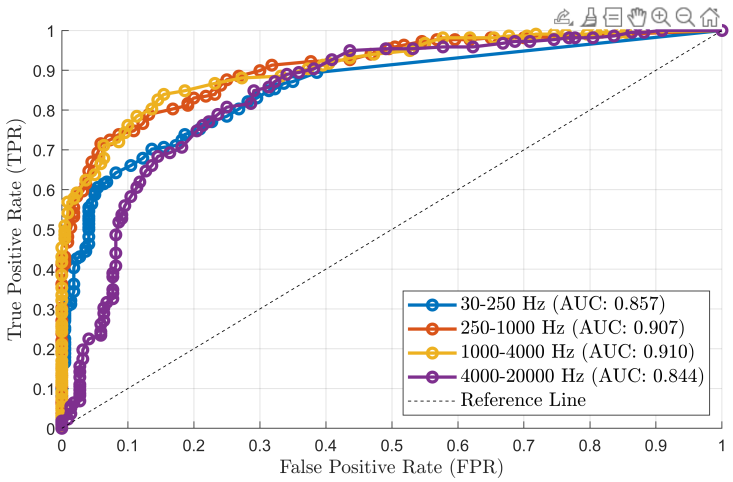

Figure A.58: The ROC curve for an STA of 3 minutes and an LTA of 180 minutes

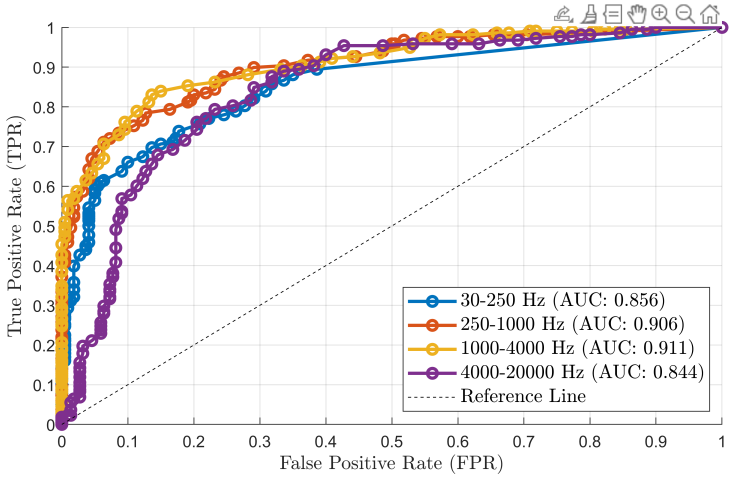

Figure A.59: The ROC curve for an STA of 3 minutes and an LTA of 190 minutes

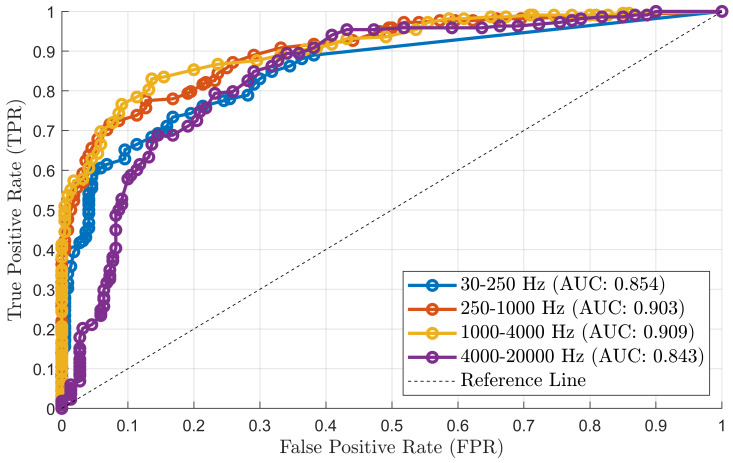

Figure A.60: The ROC curve for an STA of 3 minutes and an LTA of 200 minutes

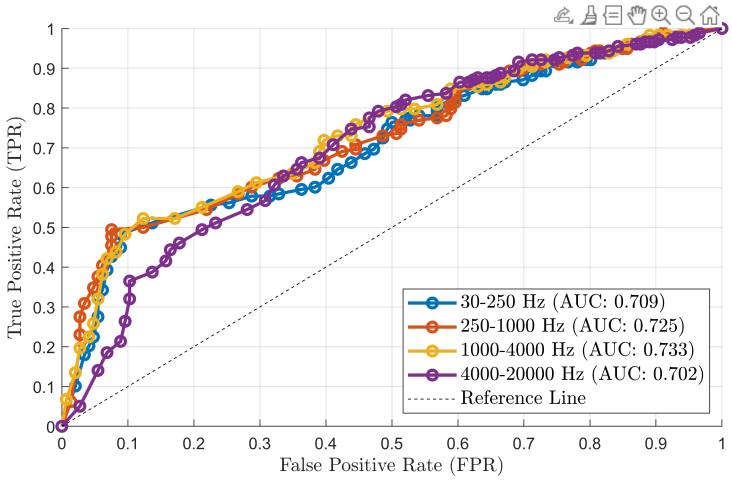

Figure A.61: The ROC curve for an STA of 4 minute and an LTA of 10 minutes

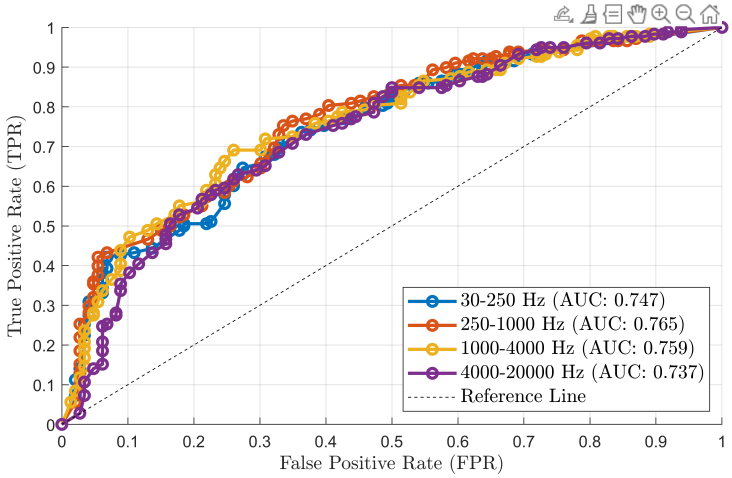

Figure A.62: The ROC curve for an STA of 4 minute and an LTA of 20 minutes

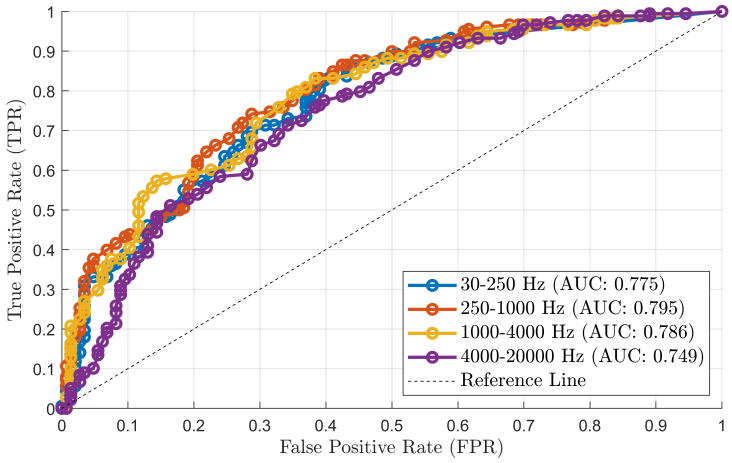

Figure A.63: The ROC curve for an STA of 4 minute and an LTA of 30 minutes

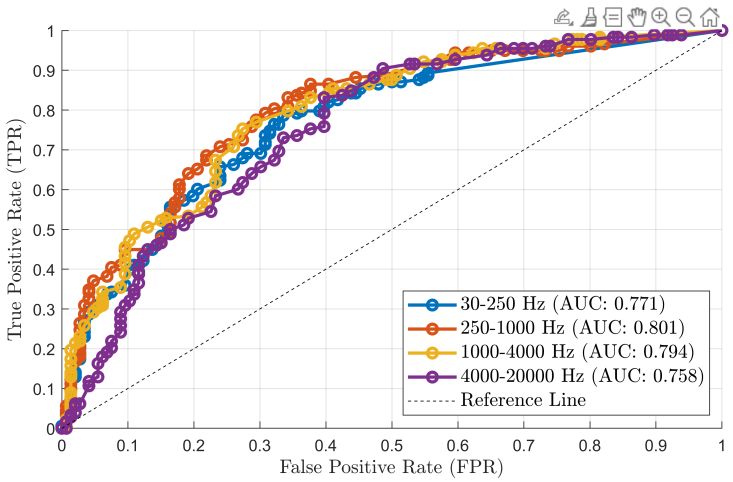

Figure A.64: The ROC curve for an STA of 4 minute and an LTA of 40 minutes

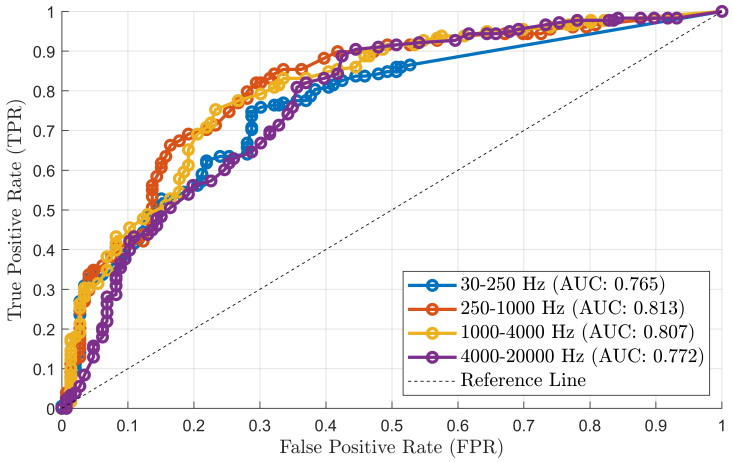

Figure A.65: The ROC curve for an STA of 4 minute and an LTA of 50 minutes

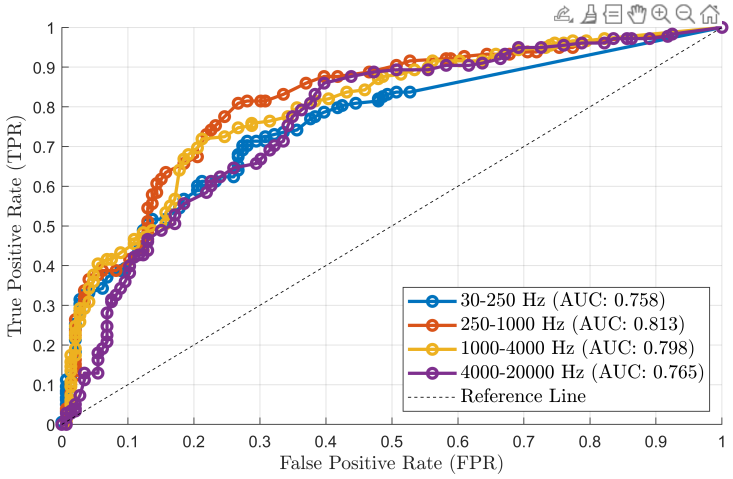

Figure A.66: The ROC curve for an STA of 4 minute and an LTA of 60 minutes

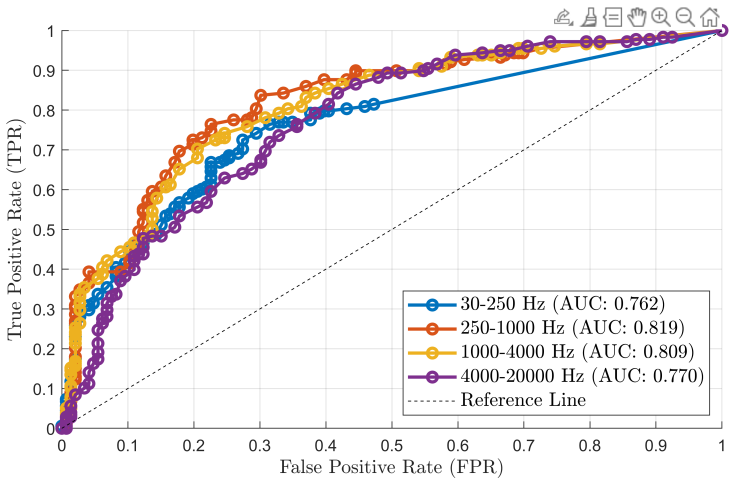

Figure A.67: The ROC curve for an STA of 4 minute and an LTA of 70 minutes

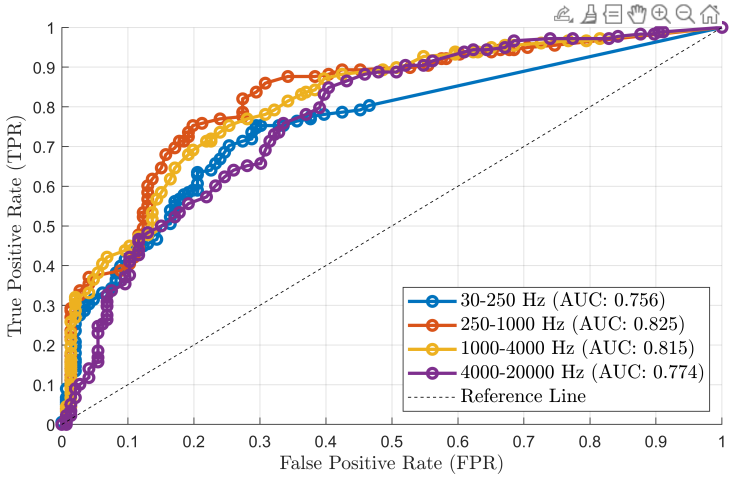

Figure A.68: The ROC curve for an STA of 4 minute and an LTA of 80 minutes

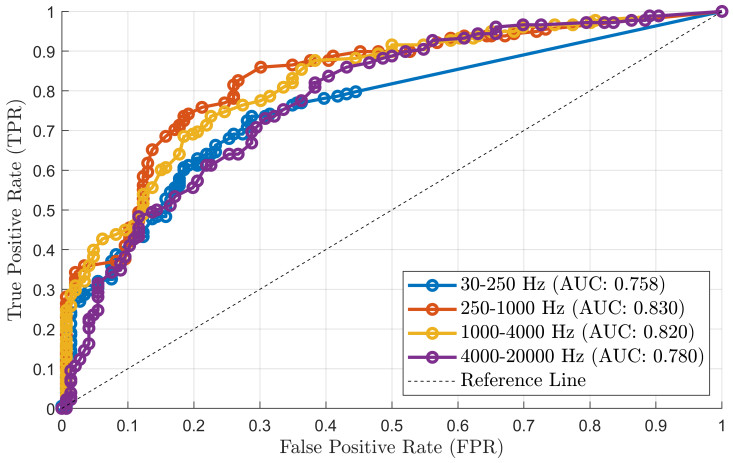

Figure A.69: The ROC curve for an STA of 4 minute and an LTA of 90 minutes

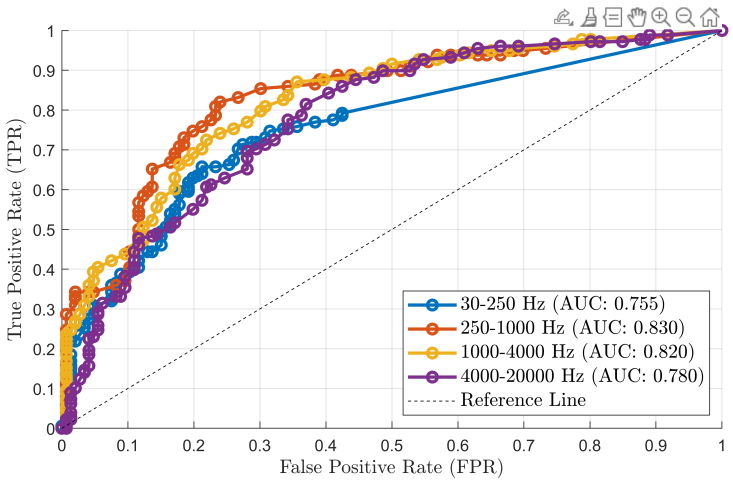

Figure A.70: The ROC curve for an STA of 4 minutes and an LTA of 100 minutes

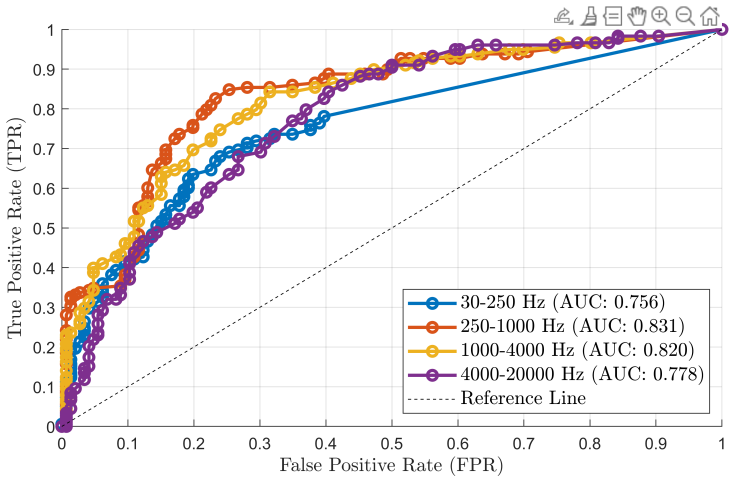

Figure A.71: The ROC curve for an STA of 4 minutes and an LTA of 110 minutes

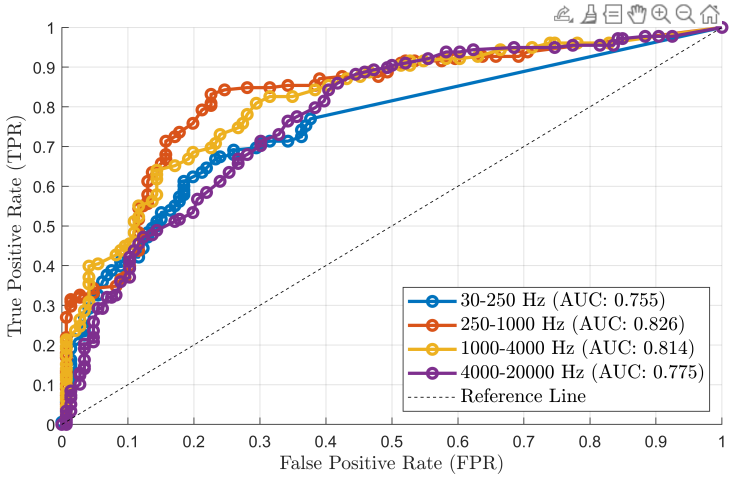

Figure A.72: The ROC curve for an STA of 4 minutes and an LTA of 120 minutes

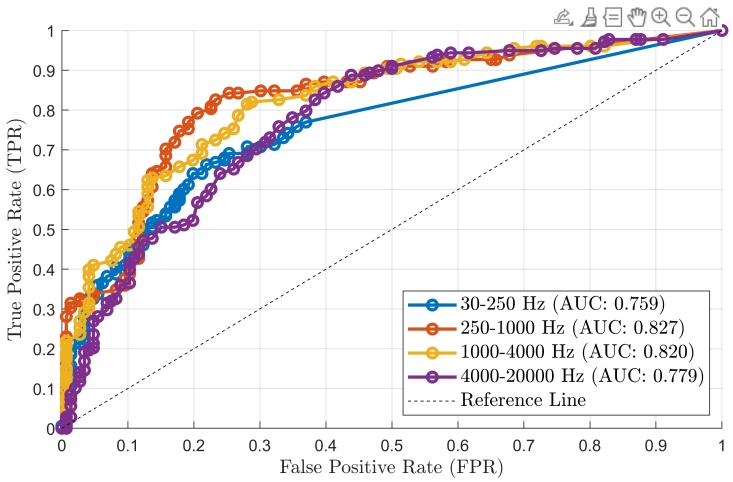

Figure A.73: The ROC curve for an STA of 4 minutes and an LTA of 130 minutes

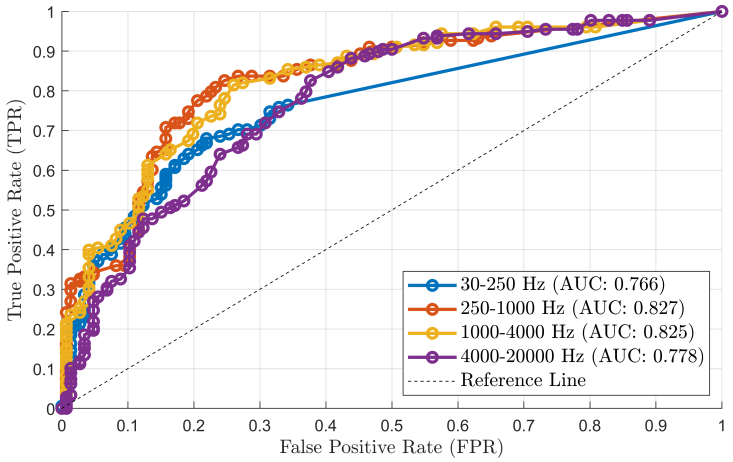

Figure A.74: The ROC curve for an STA of 4 minutes and an LTA of 140 minutes

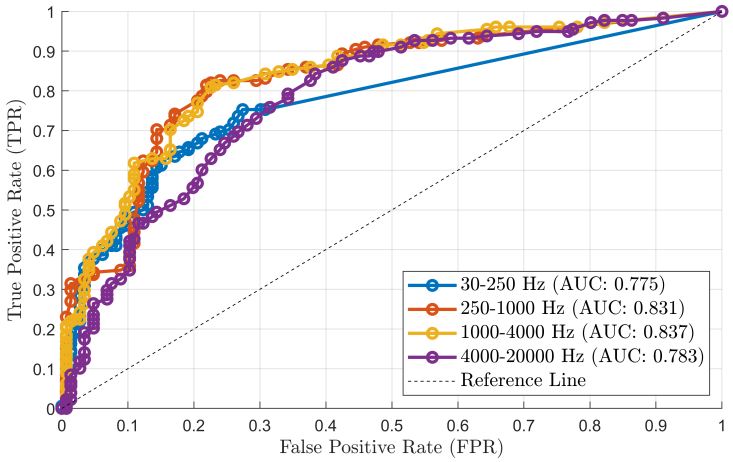

Figure A.75: The ROC curve for an STA of 4 minutes and an LTA of 150 minutes

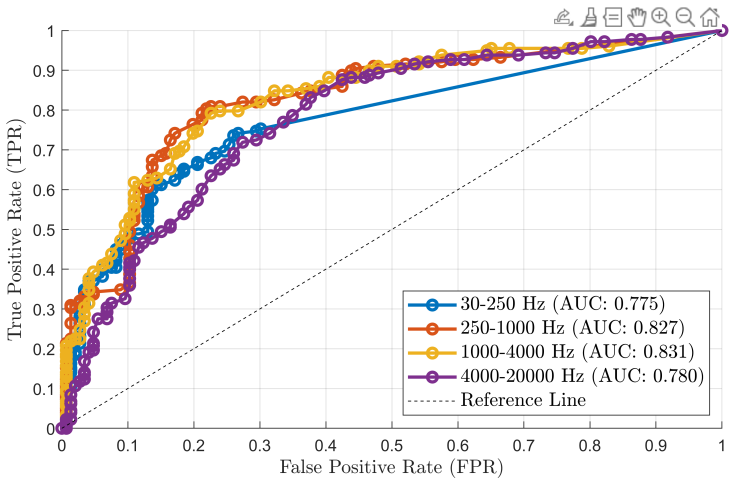

Figure A.76: The ROC curve for an STA of 4 minutes and an LTA of 160 minutes

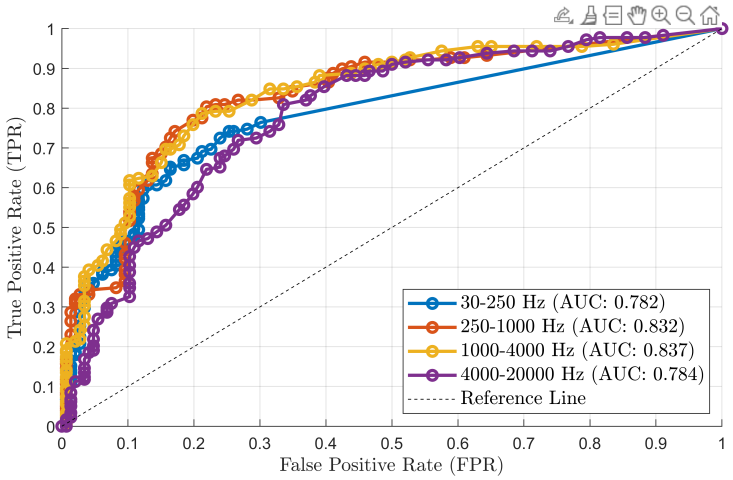

Figure A.77: The ROC curve for an STA of 4 minutes and an LTA of 170 minutes

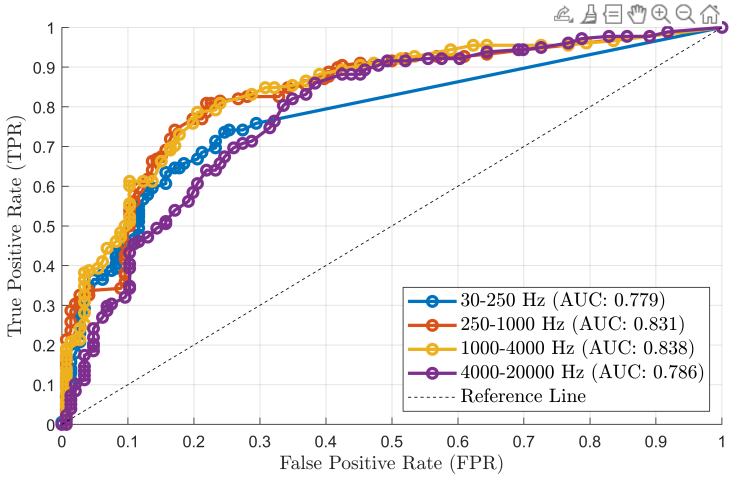

Figure A.78: The ROC curve for an STA of 4 minutes and an LTA of 180 minutes

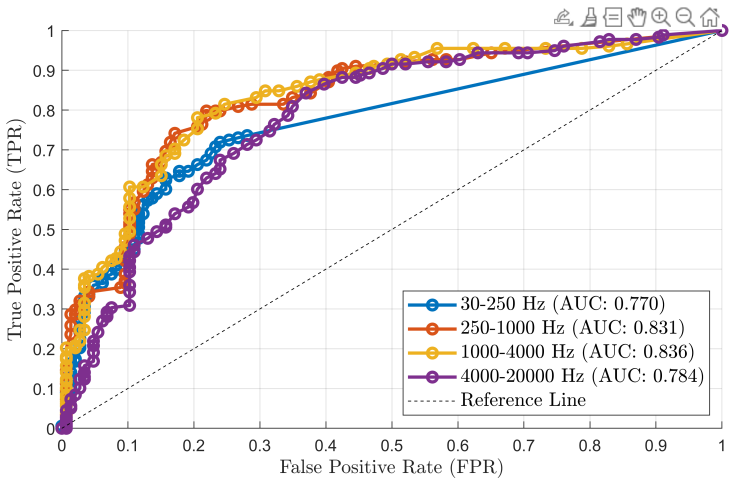

Figure A.79: The ROC curve for an STA of 4 minutes and an LTA of 190 minutes

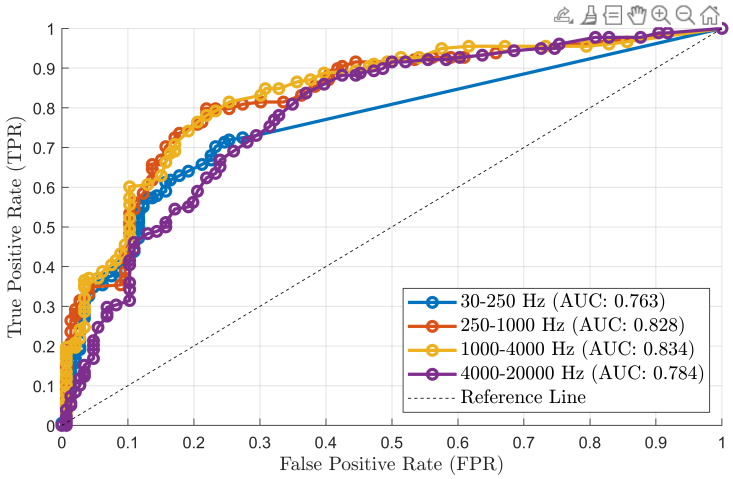

Figure A.80: The ROC curve for an STA of 4 minutes and an LTA of 200 minutes

DEPARTMENT OF ARCHITECTURE AND CIVIL ENGINEERING
CHALMERS UNIVERSITY OF TECHNOLOGY
Gothenburg, Sweden
www.chalmers.se

CHALMERS
UNIVERSITY OF TECHNOLOGY